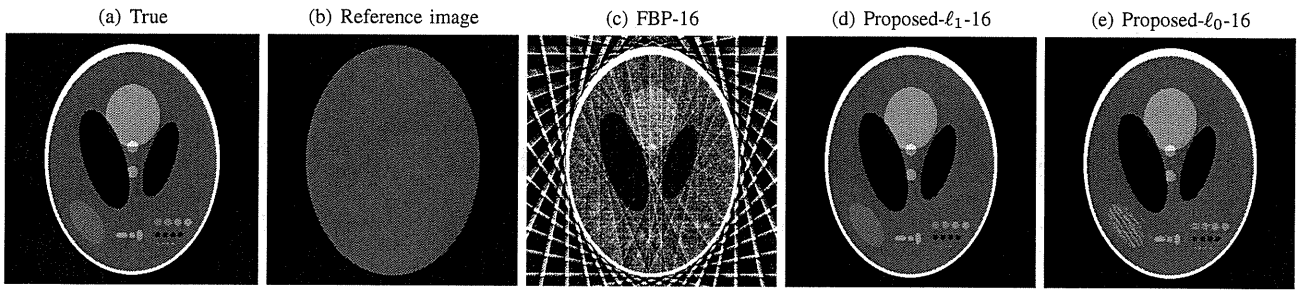

Fig. 2. (a) Modified Shepp-Logan phantom and image reconstructed from 16 projection views using (c) standard FBP algorithm and the proposed method using reference image in (b) with ℓ_1 and ℓ_0 norms in (d) and (e) , respectively.

REFERENCES

[1] E. Y. Sidky, C.-M. Kao and X. Pan, "Accurate image reconstruction from few-views and limited-angle data in divergent-beam CT," *J. X-Ray Sci. Technol.*, vol. 14, pp. 119-139, 2006

[2] J. Tang, B. E. Nett, and G.-H.Chen, "Performance comparison between total variation (TV)-based compressed sensing and statistical iterative reconstruction algorithms," *Phys. Med. Biol.*, vol. 54, pp. 5781-5804, 2009.

[3] J. Trzasko and A. Manduca, "Highly undersampled magnitic resonance image reconstruction via homotopic ℓ_0 minimization," *IEEE Trans. Med. Imag.*, vol. 28, pp. 106-121, 2009.

[4] H. Yu and G. Wang, "A soft-threshold filtering approach for reconstruction from a limited number of projections," *Phys. Med. Biol.*, vol. 55, pp. 3905-3916, 2010.

[5] M. Li, H. Kudo, J. Hu and R. H. Johnson, "Improved iterative algorithm for sparse object reconstruction and its performance evaluation with micro-CT data," *IEEE Trans. Nucl. Sci.*, vol. 51, pp. 659-666, 2004.

[6] D. P. Bertsekas, *Nonlinear Programming*. Massachusetts: Athena-Scientific, 1995.

OPEN ACCESS Freely available online

PLoS one

Spatial Frequency-Based Analysis of Mean Red Blood Cell Speed in Single Microvessels: Investigation of Microvascular Perfusion in Rat Cerebral Cortex

Joonas Autio[1☯¤], Hiroshi Kawaguchi[1☯], Shigeyoshi Saito[1], Ichio Aoki[1], Takayuki Obata[1], Kazuto Masamoto[1,2], Iwao Kanno[1*]

1 Department of Biophysics, Molecular Imaging Center, National Institute of Radiological Sciences, Anagawa, Chiba, Japan, **2** Center for Frontier Science and Engineering, University of Electro-Communications, Chofu, Tokyo, Japan

Abstract

Background: Our previous study has shown that prenatal exposure to X-ray irradiation causes cerebral hypo-perfusion during the postnatal development of central nervous system (CNS). However, the source of the hypo-perfusion and its impact on the CNS development remains unclear. The present study developed an automatic analysis method to determine the mean red blood cell (RBC) speed through single microvessels imaged with two-photon microscopy in the cerebral cortex of rats prenatally exposed to X-ray irradiation (1.5 Gy).

Methodology/Principal Findings: We obtained a mean RBC speed (0.9±0.6 mm/sec) that ranged from 0.2 to 4.4 mm/sec from 121 vessels in the radiation-exposed rats, which was about 40% lower than that of normal rats that were not exposed. These results were then compared with the conventional method for monitoring microvascular perfusion using the arteriovenous transit time (AVTT) determined by tracking fluorescent markers. A significant increase in the AVTT was observed in the exposed rats (1.9±0.6 sec) as compared to the age-matched non-exposed rats (1.2±0.3 sec). The results indicate that parenchyma capillary blood velocity in the exposed rats was approximately 37% lower than in non-exposed rats.

Conclusions/Significance: The algorithm presented is simple and robust relative to monitoring individual RBC speeds, which is superior in terms of noise tolerance and computation time. The demonstrative results show that the method developed in this study for determining the mean RBC speed in the spatial frequency domain was consistent with the conventional transit time method.

Citation: Autio J, Kawaguchi H, Saito S, Aoki I, Obata T, et al. (2011) Spatial Frequency-Based Analysis of Mean Red Blood Cell Speed in Single Microvessels: Investigation of Microvascular Perfusion in Rat Cerebral Cortex. PLoS ONE 6(8): e24056. doi:10.1371/journal.pone.0024056

Editor: Timothy W. Secomb, University of Arizona, United States of America

Received February 16, 2011; **Accepted** August 3, 2011; **Published** August 24, 2011

Funding: The study was partly supported by the Scandinavia-Japan Sasakawa Foundation (JA), the Special Coordination Funds for Promoting Science and Technology (KM), and KAKENHI from Japan Society for the Promotion of Science in Japan (TO and HK). The funders had no role in study design, data collection and analysis, decision to publish, or preparation of the manuscript.

Competing Interests: The authors have declared that no competing interests exist.

* E-mail: kanno@nirs.go.jp

☯ These authors contributed equally to this work.

¤ Current address: Department of Neurobiology, A. I. Virtanen –Institute, University of Eastern Finland, Kuopio, Finland

Introduction

Prenatal exposure to X-ray irradiation is a leading cause of postnatal development deficits such as a decrease in brain size and retardation of behavioral and mental activity [1]. Recently, we found that X-ray irradiation exposure (1.5 Gy) on the 15th day of pregnancy impaired the development of vascular endothelial cells and cerebral arteriogenesis in postnatal rat brains [2]. Further, following prenatal exposure to irradiation, newborn rats showed reduced cerebral blood flow (CBF), which was only half of that observed in age-matched non-exposed rats [2]. These findings suggest that immature development of the brain vasculature, including cerebral hypo-perfusion, is of etiological importance in the delayed development of the central nervous system (CNS) observed in subjects following prenatal exposure to X-ray irradiation.

Because the CBF reflects a product of cortical blood volume per unit tissue volume and cross-sectional blood velocity in the vessels, the cerebral hypo-perfusion observed in the exposed subjects could be due to low blood volume (i.e., decrease in capillary density) in the parenchyma tissue relative to non-exposed subjects, or it could be due to a decrease in blood velocity through the parenchyma capillaries. In the former case, low blood volume may result from an immature development of the microvasculature. In the latter case, a decline in blood velocity can be interpreted as a higher resistance in the cerebral circulation in the exposed subjects, which can be attributed to a narrow lumen space of cerebral arteries or low demand of metabolic activity in parenchyma tissue. In either case, it is necessary to measure the blood velocity in the parenchyma capillaries directly to further determine the source of the hypo-perfusion observed in the prenatal exposed subjects.

Using a variety of fast-scanning optical microscopic techniques, previous studies have shown that the mean red blood cell (RBC) speed in cortical microvessels ranged from 0.4 to 1.5 mm/sec in anesthetized rats [3-7]. However, these studies were limited to microvessels located on the cortical surface, but not in parenchyma capillaries, where neural processes and metabolic activity occur. Alternatively, Kleinfeld et al. [8] first used two-photon microscopy to directly visualize RBC movement through the parenchyma capillaries up to a depth of 600 μm. Two-photon microscopy has an increase in the depth of tissue penetration into biological tissue as compared to other most commonly used optical microscopes [9,10]. The near-infrared excitation wavelengths used in two-photon microscopy allows for high penetration of the light into the tissue due to low absorption and scattering effects [11]. However, the depth penetration of two-photon imaging is decreased in circumstances of increased tissue absorption and scattering [12,13], which makes analyzing small targets, i.e., moving RBCs, difficult, such as in disease model animals where the scattering and/or absorption of light by the tissue is high.

To overcome the potential limitations in analyzing RBC speed from poor contrast-to-noise ratio images in disease model animals, we developed an analytical method based on a two-dimensional fast Fourier transform (FFT) approach. This method is similar to that used in a recent study by Drew et al. [14] who used the Radon transform to characterize the spatial pattern of the RBC traces. In their study, it was shown that a coordinate-transform method is superior in terms of noise tolerance for the extraction of RBC slope from line-scanned vascular images, as compared to the original approach with a singular value decomposition (SVD) method [8]. The 2D FFT approach presented here directly utilized raw line-scanned images, which contained vascular and non-vascular signals. The method was then applied to determine the mean RBC speed in the cerebral cortex in rats receiving prenatal X-ray irradiation (1.5 Gy) according to our previous study [2]. These results were further compared with the conventional method for determining the microvascular perfusion based on the arteriovenous transit time (AVTT) [15-17] in both X-ray exposed and non-exposed rats. Using this new analytical approach to determine the microvascular RBC speed and conventional AVTT measurements, we consistently found approximately 40% lower microvascular perfusion in the cerebral cortex of prenatally exposed rats as compared to non-exposed rats.

Results

RBC speed in single microvessels

Figure 1A shows a representative raw image of an RBC trace using the two-photon line-scanning method at a single location in the parenchyma microvessel. Dark streaks in the image represent the unlabelled RBC moving through the vessel in a longitudinal direction. Figure 1B shows a power spectrum image calculated from the 512 by 512 pixel image in Fig. 1A. The oblique shape in the FFT image is elongated in the direction perpendicular to the dark streaks in the original image. Changing to polar coordinates in the frequency space, the power spectrum was summed along lines of θ (Fig. 1C, and see Eq. 2). The angle corresponding to the peak of the radial spectrum was then used to calculate the mean RBC speed with Eq.1. The mean RBC speed in this representative image was calculated to be 1.1 mm/sec. Under our experimental protocol, the time required to compute the mean RBC speed was 0.60 sec per image with the proposed method, which was faster than a method employing SVD (4.74 sec per image), and almost equivalent to a method using the Radon transform (0.75 sec per image). The population data (121 vessels from four exposed rats) showed that the obtained mean RBC speed ranged from 0.2 to 4.4 mm/sec, and the mean of all measurements was 0.9±0.6 mm/sec (Fig. 2).

Cortical AVTT measurements

Figure 3A shows an image of the appearance time measured on the cortical surface of a representative non-exposed animal. Based on the spatial continuity of the appearance over time, arterial and venous segments were determined (37,638 and 97,272 pixels in this representative image, which accounted for 14% and 37% of

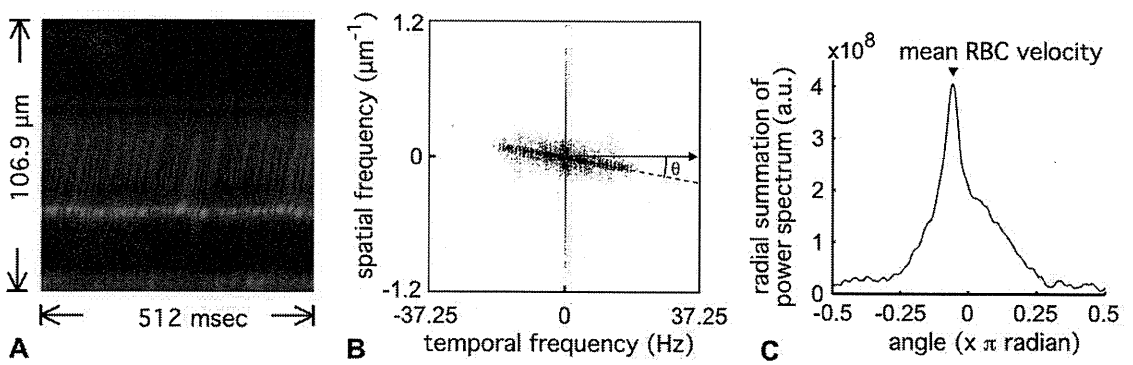

Figure 1. Representative image and measurement of RBC speed in single microvessels of the exposed animals. (A) A raw image of RBC moving through a microvessel was obtained using a line-scan mode with two-photon microscopy. The representative image showed 512 lines captured at the center of the target microvessel in parallel to the longitudinal direction. The x-axis represents Δt of 1 msec/pixel (time domain), and the y-axis is Δx of 0.20 μm/pixel (spatial domain). The green color represents the measured intensity of the fluorescent signal that originated from the injected plasma marker. Dark streaks observed around the center of the image were mainly caused by unlabelled RBC motions, and their slopes reflect a speed of the RBC motions that were parallel to the vessel length (a scan direction). (B) Power spectrum image. The image represents a FFT image constructed from the original 512 by 512 pixel image (A). The power spectrum was used to characterize a periodic pattern of the pixel intensity distribution represented in the raw image (A). A slanted line reflects a direction preference, perpendicular to the RBC traces (i.e., a slope of dark streaks), which appeared in the original image. The angle between this slanted line and the temporal axis was used to calculate the mean RBC speed (see text). (C) The spatial pattern of the pixel intensity distribution converted by the FFT analysis. Summation of the power spectrum at each angle was calculated for all directions (-0.5 to 0.5 π), and the angle that had the maximum power (arrow head) was used to calculate mean RBC speed (1.1 mm/sec in this representative image) (see Eq. 1).
doi:10.1371/journal.pone.0024056.g001

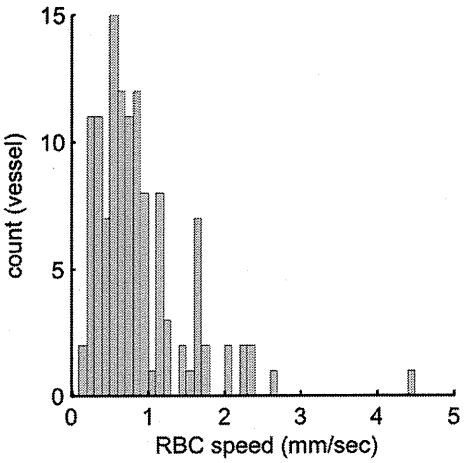

Figure 2. Mean RBC speed in single microvessels. The histogram shows the frequency distribution of the mean RBC speed obtained from all 121 vessels in the exposed rats (N = 4). The mean RBC speed ranged from 0.2 to 4.4 mm/sec (minimum to maximum), and the mean of all measurements was 0.9±0.6 mm/sec.
doi:10.1371/journal.pone.0024056.g002

total pixel numbers, respectively, Fig. 3B). In this rat, the mean appearance time was 0.29±0.28 and 1.43±0.48 sec in the arterial and venous segments, respectively (see Fig. 3C). Consequently, the AVTT was calculated as 1.14 sec. In addition, the median of the appearance time (0.21 and 1.33 sec in arterial and venous segments, respectively) was used to compare transit times. The AVTT was 1.12 sec, which was similar to the results obtained from the mean value. Therefore, the AVTT was calculated using the mean values.

A clear separation in the appearance time between the arterial and venous segments was consistently observed in all four exposed animals (Fig. 4A). The mean area of the observed vascular segments was 15,789±10,909 and 34,355±11,539 pixels in the arterial and venous segments, respectively, corresponding to 6±4% and 13±4% of the total number of pixels (262,144) in the image, respectively. In contrast, the results for the non-exposed animals were 12±4% and 30±9% of the pixels occupied by the arterial and venous segments, respectively. Interestingly, the mean ratio of the areas covered by the arterial and venous segments was similar for the exposed (1:2.2) and non-exposed (1:2.4) animals.

The mean of the AVTT was 1.9±0.6 sec in exposed animals, which was significantly longer than that of non-exposed animals (1.2±0.3 sec, Fig. 4B). To further compare the baseline capillary blood velocities in the exposed and non-exposed animals, the inverse of the mean AVTT was plotted in Figure 5B. Assuming that the tissue blood volume (i.e., a total vessel length) was the same for the two groups, the observed inverse transit times may reflect the mean of capillary blood speed through the parenchyma tissue. Comparison of the inverse transit times for the non-exposed and exposed groups found a ratio of 66%. A comparison for the mean capillary RBC speed measured in the present (exposed) and previous (non-exposed) studies found a similar ratio of 60% (Fig. 5A).

Discussion

Technical issues of frequency-based image analysis

Using the spatiotemporal frequency-based approach, the automated image analysis method was developed to measure the mean RBC speed from the population of RBCs moving in single microvessels of the cerebral cortex (Figs. 1, 2). The advantages of the present approach are the following: i) the mean RBC speed can be determined from images that contain a population of RBCs without distinguishing individual cells, such as for low signal-to-noise images, ii) the computation time required for the calculation is significantly improved relative to the previously-reported method with SVD, and iii) the algorithm is simple and no prior information is required, which makes it easy to implement. Based on a space-time image obtained by a line-scanning of RBC motions along the vessel, early studies have established a method that enabled RBC speed to be determined from the slope of the

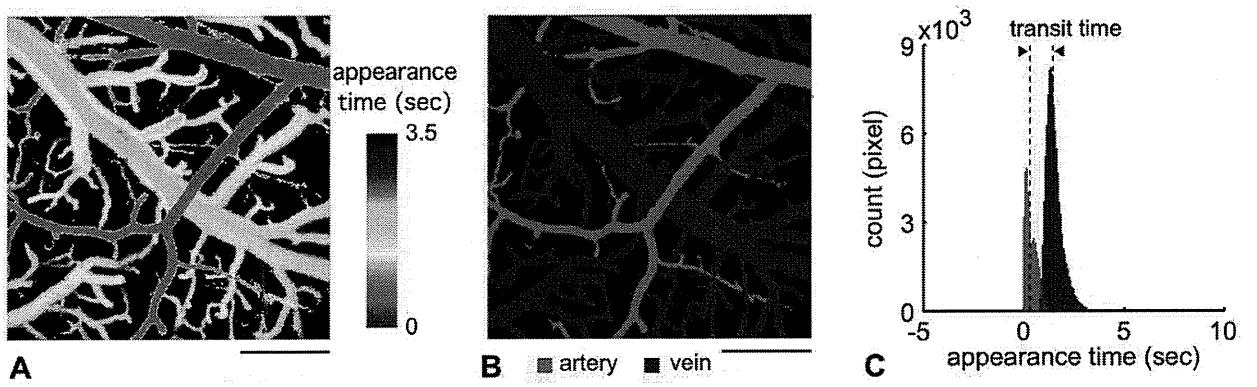

Figure 3. Representative image and measurement of AVTT. (A) A representative image of the appearance time obtained from one animal. Time-lapse imaging was performed at the cortical surface with a frame-capture rate of 14.2 frame/sec. The field of view was 512 by 512 pixels, and in-plane resolution was 3.6 μm/pixel. The pixel-basis analysis of appearance time was performed (see text). The image showed a continuity of appearance time in each vascular segment. An early appearance time (red) mostly represented an arterial flow, whereas a late appearance time (yellow to blue) resulted from venous flow. The color bar indicates the image acquisition time. Scale bar: 0.5 mm. (B) Segmentation of arterial and venous compartments. The arterial (red) and venous (blue) blood vessel areas were determined based on the spatial continuity of the appearance time observed along a longitudinal direction of the vessels (see text). Scale bar: 0.5 mm. (C) AVTT. The histogram represents the frequency distribution of appearance time observed in respective arterial (red) and venous (blue) areas. A total of 37,638 and 97,272 pixels were counted for arterial and venous segments, respectively, in this representative animal. Mean appearance time was observed as 0.29±0.28 and 1.43±0.48 sec in the arterial and venous segments, respectively, and thus, AVTT was 1.14 sec (a width between dashed vertical lines).
doi:10.1371/journal.pone.0024056.g003

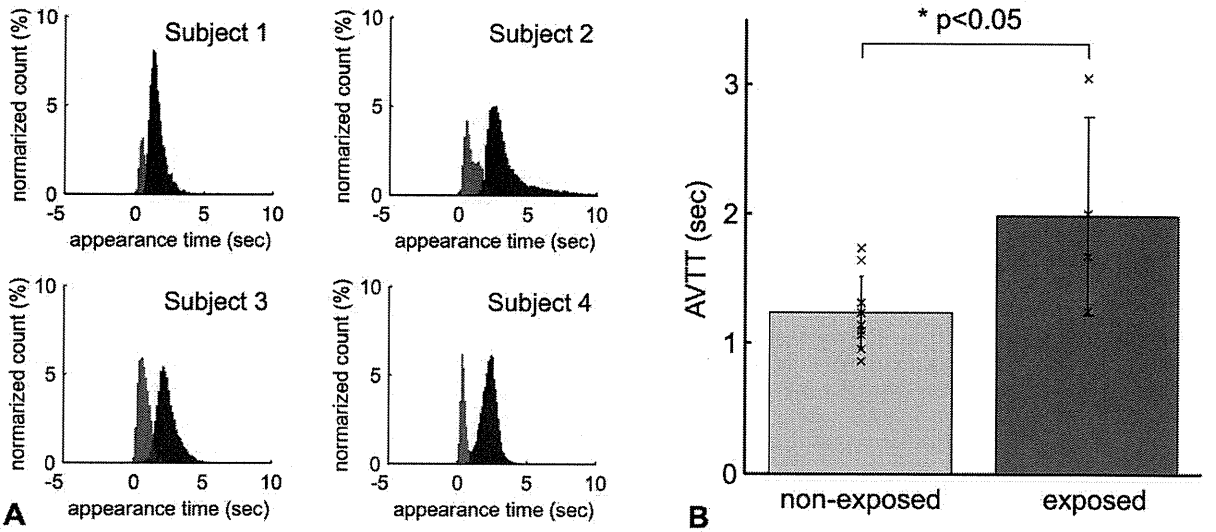

Figure 4. A comparison of mean AVTT. (A) The normalized histogram of the appearance time in all exposed rats (N = 4). The consistent distribution pattern of the appearance time was observed for both the arterial (red) and venous (blue) segments. (B) Population data on mean AVTT. Mean of AVTT was 1.2±0.3 and 1.9±0.6 sec in non-exposed (N = 9) and radiation exposed animals (N = 4), respectively. There were statistically significant differences between the two groups ($p<0.05$).
doi:10.1371/journal.pone.0024056.g004

RBC displacement per certain time intervals (i.e., scanning intervals) [4,17]. Later studies have presented a variety of image-based approaches, using SVD [8,18], two-dimensional image autocorrelation [19], Hough transform [20], and Radon transform [14,21], to extract the average slope. In particular, the SVD and Radon transform methods have been widely used to automatically determine dynamic changes in brain capillary RBC speeds [22-24]. For dynamic imaging, computation time is a key issue for achieving real time monitoring. We compared the computation time required for the method proposed in this paper and these alternative methods, and found that under our experimental conditions the proposed method is about 8 times faster than the SVD and equivalent to or slightly faster (1.25 times) than the Radon transform methods. With a Radon transform approach and simulated data degraded with various levels of noise, Drew et al. [14] showed that the coordinate-transform method has some advantages over the SVD. The 2D FFT presented here utilized the periodic pattern of the pixel intensity distribution (i.e., RBC streaks), and thus is relatively insensitive to signal arising from the non-vascular areas. This means that there is no need to crop the vascular areas from the raw image to detect RBC streaks. This is demonstrated in our supplementary results where it is shown that when the image covered relatively large non-vascular areas, the present method found a single unique peak, whereas the Radon

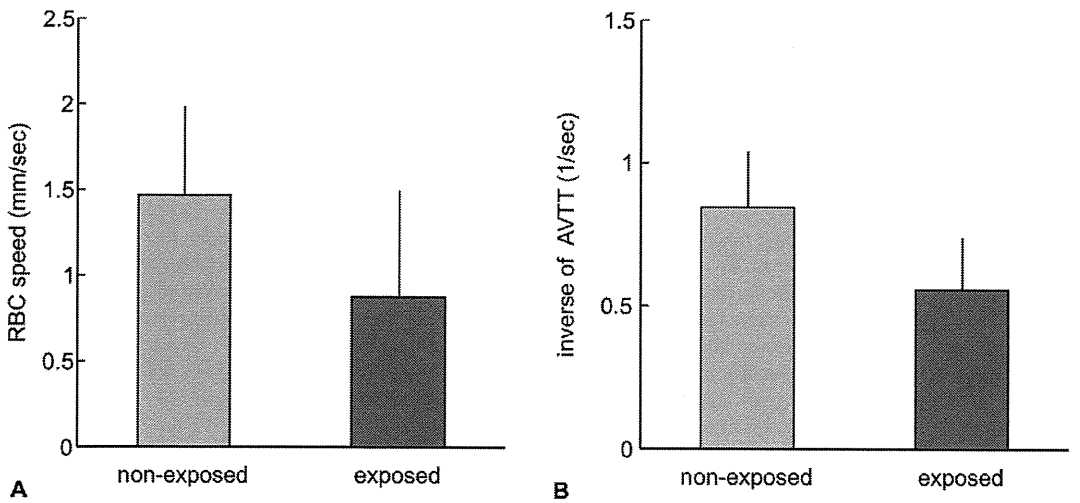

Figure 5. A comparison of capillary blood speeds. (A) Mean capillary RBC speed. The mean capillary RBC speed measured in the present study for the exposed animals (N = 4) was 40% lower than that for the non-exposed animals measured in a previous study (modified from [30]). (B) Inverse of the mean AVTT. The inverse of the mean AVTT of the exposed animals was 34% lower than that of the non-exposed animals. The ratio of exposed to non-exposed animal results was similar for both data sets.
doi:10.1371/journal.pone.0024056.g005

transform method did not (Fig. S1). An algorithm that reliably provides a unique peak is important for running the automated analysis, and no requirement to crop the images would be beneficial in reducing user bias and the number of steps in image processing. Further, specificity of the present method to the RBC streaks in the image could be used to reduce non-vascular signals by applying a bandpass filter in the frequency domain. This approach would be also useful as a pre-processing step (denoising) prior to identifying individual RBCs for counting [25], fitting [26], and tracking [27-29].

In contrast, one limitation of the frequency-based approach is that the method is only applicable to an image that contains a single pattern of RBC traces. If the images contain multiple patterns of RBC traces, such as due to temporal fluctuations and spatial variations of RBC movements through a single microvessel, it is necessary to assign an appropriate region of interest and time window (see also Fig. S2). The spatiotemporal dynamics of the RBC behaviors, such as during spontaneous fluctuations and response to neural functions in both prenatal exposed and non-exposed subjects, must be investigated in future studies.

Radiation effects on cerebral microcirculation

We observed that the mean RBC speed was 0.9±0.6 mm/sec in the exposed rats (Fig. 2), which was approximately 40% lower than that in isoflurane-anesthetized normal rats (Fig. S3 modified from [30]). Other studies have shown that the mean RBC speed in the microvessel on the cortical surface and parenchyma tissue ranged from 0.4 to 1.5 mm/sec as measured in anesthetized rats [3-8,22,31]. This large variation could be due to animal physiology from various labs and/or methods used to determine the RBC speed. In our previous study, we found that anesthesia significantly impacted the mean RBC speed in cortical microvessels; 0.4±0.4 mm/s and 1.5±0.4 mm/s under alpha-chloralose and isoflurane, respectively [30]. These findings are consistent with other reports that examined the anesthesia-dependence of CBF in rats [32,33]. The CBF in the somatosensory cortex of rats under isoflurane was shown to be equivalent to the non-anesthetized awake rats (130-150 ml/ 100g/ min) [34], indicating that isoflurane anesthesia is the preferred anesthetic to preserve normal CBF characteristics [35]. Using a high-speed confocal laser scanning microscope, it has been shown that the high-frame rate measurements (500 frame/s) recorded a 2.2 mm/s average for RBC speed (ranged from 0.8 to 6.6 mm/sec) in rats and mice [36,37]. Therefore, our RBC measurements were further compared with the conventional method for microvascular perfusion measurements [15,16]. In the present study, a fluorescent dye was injected into the femoral vein to measure the cortical AVTT. During its passage to the measurement site in the cortex the concentration of the dye will be diluted with blood, and this might complicate the separation of artery and venous segments. To avoid this possibility, we used the earliest image where the fluorescent signal appeared in a particular vessel for artery-vein segmentation (Fig. 3). Other studies have injected dye directly into the internal carotid artery [38,39], which allows the arrival of the dye at the imaging area of the cortex to be approximated by an impulse function (Dirac's delta). From preliminary tests with dye injection into the internal carotid artery, we found the mean AVTT to be 1.3±0.6 sec for the normal rats (N = 3), which was in good agreement with the present results (1.2±0.3 sec) obtained with dye injection into the femoral vein of the non-exposed rats. The intravenous injection is less-invasive than arterial injection methods, and thus has the advantage of permitting repeated long-term measurements of cerebral microvascular perfusion [40]. As a non-invasive technique, laser-Doppler flowmetry (LDF) might be considered as a good alternative to repeated long-term CBF measurements with a dye. However, LDF measures only relative changes with respect to the baseline CBF condition and thus may not be suitable for subject comparisons of stationary CBF between normal and disease states.

For the group comparisons, we assumed that blood volume per unit tissue was equivalent for the exposed and non-exposed animals. However, if the total vessel length is longer in the exposed rats, this might explain the longer mean AVTT that was observed. However, since our MR data showed that the cortical thickness in the exposed animals was only 36% of that of age-matched non-exposed animals (data not shown), this possibility can be ruled out. Measurements of the RBC speed and inverse of mean AVTT consistently showed an approximately 40% decline in cortical microvascular perfusion in the exposed rats in comparison to the non-exposed rats (Figs. 4, 5). These findings are also in good agreement with our previous measurements of CBF using magnetic resonance imaging (MRI) that showed that exposed newborn rats (postnatal 2 weeks) had approximately 50% of the CBF of the age-matched non-exposed rats [2].

The cerebral hypo-perfusion observed in the prenatal exposed rats could be due to the immature development of vascular systems and/or secondary effects of a lower energy demand in parenchyma tissue. In a previous study, with MR angiography, we found that the diameter of the middle cerebral artery was 63% smaller in the prenatally-exposed rats (0.24±0.02 mm) in comparison to the non-exposed age-matched animals (0.38±0.02 mm) [2]. In agreement with this finding, the present study showed that the area covered by arterial vessels on the cortical surface was almost half in the exposed animals relative to the non-exposed ones. Since the general physiology (MABP and heart rate) was not significantly different between the two groups, the possibility that the effects of radiation exposure on the CBF are due to general ill-health or lower cardiac output in the animals can be ruled out. Previous and present findings indicate that shrinkage of the major cerebral arteries could increase vessel resistance and result in parenchymal hypo-perfusion. Further technical improvement of cerebro-microvascular angiography would help highlight the main source of increased resistance at a microscopic scale.

In addition, no leakage of the fluorescent marker into the extravascular space was observed (data not shown), which indicates an intact blood-brain barrier (BBB) for the exposed as well as non-exposed animals. In a previous study, albumin-staining histology was performed to check the permeability of the BBB for prenatally-exposed rats [2]. The results showed that the number of albumin-positive cells in the cortex drastically decreased 2 weeks after birth for both exposed and non-exposed animals [2]. The findings also indicate that the function of the vascular endothelium (i.e., BBB permeability) developed normally for the prenatally exposed animal brains. In contrast, other studies have shown that X-ray exposure (60 Gy) of adult rats provoked disruption of BBB functions [41]. The discrepancy between the present and previous studies could be due to different dosage (1.5 Gy vs. 60 Gy) and/or age of exposure (prenatal vs. adult). In our studies, we also found that the mean density of laminin-positive cells (i.e., vascular endothelium cells) was significantly lower for the exposed (3,300 cells/mm^2) relative to the non-exposed (5,200 cells/mm^2) 2-week-old rat cortex [2]. The findings are consistent with results for adult rats and mice showing that loss of endothelial cells depends on X-ray irradiation dose and time after exposure [42,43]. Because the vascular endothelial cells belong to a category of high radiosensitivity cells [44], these observations suggest that prenatal exposure to X-ray irradiation damaged the development of vascular endothelial cells. A lack of endothelium development may further

disrupt the organization of CNS cells and networks. In this vein, an improvement or enhancement of endothelial cell growth potentially improves CNS cell development and neural connections, which may be a possible therapeutic target to prevent development defects in the prenatal exposed subjects. On the other hand, it has been shown that a density of cortical neurons and astroglia was preserved in the postnatal rats following X-ray irradiation (1.0 Gy) despite a decrease in cortical thickness [45,46]. These findings suggest that the local energy demand per unit volume was similar to that of non-exposed subjects. However, the total number of CNS cells decreased [45], and thus, the total energy level may be suppressed in exposed-animals. In this case, hypo-perfusion could result from a low metabolic demand in parenchyma tissue, which may be coupled to a total vascular length. Overall, these results strongly suggest that immature development of the brain vascular system and the related cerebral hypo-perfusion is of etiological importance in the delayed CNS development in subjects following prenatal exposure to X-ray irradiation. Future studies must address the molecular mechanism of CNS hypo-perfusion and its role in developing brains.

Conclusion

In conclusion, the present study developed a novel analytical method to determine the mean RBC speed from a large number of traces from a population of RBC images based on the 2D FFT approach. The method is simple and robust and enables automated quantification with minimum computation time. Further, the present study showed the significant decline in microvascular perfusion in the cerebral cortex of prenatal-exposed rats. These findings are consistent with our previous report [2]. Thus, the present method is valuable to further our understanding of the causal relationship between the decline of cerebral microvascular perfusion and delayed CNS development in the subjects following prenatal exposure to X-ray irradiation.

Materials and Methods

Animal preparation

The study was carried out in accordance with the recommendations in the Guide for the Care and Humane Use of Laboratory Animals of the National Institutes of Health. All experimental protocols were approved by the Institutional Animal Welfare Committee (Permit Number: 09-1008-4). In accordance with a previous study [2], two pregnant female Sprague-Dawley rats (15th day of pregnancy, Japan SLC, Hamamatsu, Japan) were irradiated with a single whole-body X-ray at a dose of 1.5 Gy (200 kVp, 20 mA, 0.5 mm Cu plus 0.5 mm Al filter). At eight to nine weeks after birth, a total of four male rats (230 to 300 g) from each breed were used for the experiments. Nine age-matched male Sprague-Dawley rats (210 to 320 g, Japan SLC, Hamamatsu, Japan) were also used as the non-exposed control group for microvascular AVTT measurements in the cerebral cortex.

The animals were anesthetized with isoflurane, and endotracheal intubation was performed to allow for mechanical ventilation. Catheters were placed into the femoral vein and artery for drug administration and for arterial blood sampling and monitoring systemic arterial blood pressure, respectively. The animal head was then fixed with stereotaxic frame (SG-3N, Narishige, Tokyo, Japan) by holding the animal nose and ears. Three needles were placed into the both sides of underarm and back for electrocardiogram (ECG) recording, and rectal temperature was maintained at 37°C. The left side of the skull over the somatosensory cortex (3 mm by 5 mm) was thinned with a dental drill. After the surgery was completed, the inspired gas was switched to a mixture of air and O_2 (30 to 35% total O_2), and the end-tidal isoflurane concentration was adjusted to 1.4%. The respiratory parameter was adjusted based on the arterial blood gas conditions: pH = 7.554±0.041, $PaCO_2$ = 32.3±1.0 mmHg, PaO_2 = 161±7 mmHg, hematocrit = 38.5±2.5%, and glucose concentration = 174±11 mg/dl in exposed group (N = 4), and pH = 7.471±0.024, $PaCO_2$ = 34.6±2.8 mmHg, PaO_2 = 136± 23 mmHg, hematocrit = 38.7±2.2%, and glucose concentration = 208±31 mg/dl in non-exposed group (N = 9). There were significant differences in the conditions of blood pH, PaO_2, and glucose concentrations between the exposed and non-exposed groups ($p<0.05$). Arterial blood pressure, measured with a blood pressure transducer (TSD104A, Biopac Systems, Inc., Goleta, CA), and heart rate, measured with an EEG amplifier (EEG100C, Biopac Systems, Inc.), were recorded throughout the experiments with a data acquisition system (MP150, Biopac Systems, Inc.) at a sampling rate of 100 Hz: mean arterial blood pressure (MABP) = 106±11 and 99±7 mmHg, and heart rate = 335±47 and 333±24 beats/min in exposed and non-exposed groups, respectively.

Measurement of microvascular RBC speed

The cortical microvasculature was imaged through a thinned skull using a two-photon laser scanning fluorescent microscope (TCS SP5MP, Leica Microsystems GmbH, Wetzlar, Germany) at 900-nm excitation (Mai Tai HP, Spectra-Physics, Santa Clara, CA) with an emission band-pass filter of 655/50 nm. Qdot 655 (1 μM in saline, Invitrogen, San Diego, CA) was intravenously injected into the animal to fluorescently label blood plasma [30]. RBC speed was measured in microvessels that had a diameter of less than 6 μm (i.e., capillaries) and a straight section at least 50 μm long, located between a depth of 50 and 300 μm from the cortical surface. For each target vessel, line scanning was repeatedly performed along the length of the vessel at a rate of 1-4 lines/ms, and a total of 512 lines were used to make a single image (i.e., 512 by 512 pixels, see also Fig. 1A). The image consists of an x-axis as the time domain (0.25-1 ms/pixel, Δt) and y-axis as the spatial domain (0.06-0.20 μm/pixel, Δx). The field of view and line-scan average were manually adjusted (i.e., 2-8 scan averages were typically performed with a scan speed of 0.125 ms/line). By setting 512 pixels along the horizontal axis (Δt), the temporal window was accordingly 128-512 ms, which allowed accurate calculation of the RBC speed under our experimental conditions. However, the window size is not limited. Depending on the line-scan average, an even shorter time-window (e.g., 32 pixels) is also possible (Fig. S2).

Mean RBC speed (v) was determined with the following equations:

$$v = |\mathbf{v}| = \left|\frac{\Delta x}{\Delta t}\cot\theta\right|, \quad (1)$$

where θ is the angle between the temporal frequency axis and a line perpendicular to the streaks (see Fig. 1B), and Δx and Δt are the spatial and temporal sampling intervals (i.e., a pixel width), respectively. Since Δx and Δt in Eq. (1) are given by the image acquisition parameters, θ is the only quantity that directly reflects the RBC speed. The angle θ was automatically calculated by detecting the angle having the maximum summation (g) of the power spectrum across all directions (from -0.5π to +0.5π) with a resolution of π/180 around a center of the frequency space (see Fig. 1C):

$$g(\theta) = \max_{\theta\in(-0.5\pi,0.5\pi)} \int_0^R F(r,\theta)dr, \quad (2)$$

where F(r, θ) is the transformation of a power spectrum image from Cartesian to polar coordinates. Two-dimensional linear interpolation was applied in the coordinate transformation. R was half of the pixel number, 255 in this study.

Measurement of the AVTT

Time-lapse imaging of the cortical surface vasculature was performed at a rate of 7.1, 9.5, or 14.2 frame/sec using a single-photon excitation mode (488-nm Argon laser). The image was 512 by 512 pixels, and the in-plane resolution was 3.6 μm/pixel. Immediately after the initiation of time-lapse imaging (within 10 sec), a bolus injection of Qdot 655 (1 ml/kg body weight) was administered in the femoral vein. AVTT was determined by imaging plasma markers but not RBC. Because negligible differences in the AVTT were observed between the plasma and RBC markers (data not shown), the equivalent flow characteristics of the plasma and RBC were assumed in the experimental conditions in the comparison of the measured RBC speed using conventional microvascular perfusion measurements. A median filter was first applied to reduce the shot noise of the detector (photomultiplier). AVTT was then calculated by subtracting the appearance time of the fluorescent signals determined at venous segments by those of arterial segments. The appearance time is the earliest time point that both target pixel intensity and the subsequent five time-point intensities surpassed a threshold level (i.e., mean + 2 S.D. of pre-injection baseline intensity). The baseline intensity was calculated by averaging all intensities measured during the pre-injection periods on a single pixel basis. If there were no time-points that surpass the threshold, that pixel was excluded from further analysis. Finally, arterial and venous segments were manually extracted based on a spatial continuity of the measured appearance time along a longitudinal direction of the vessels, and the appearance time of each segment was reported by averaging all pixel data of the respective segments. Data were presented as mean±S.D. across the animals unless otherwise specified, and a Student's t-test was performed for statistical analysis to compare the radiation-exposed and non-radiation group data.

Supporting Information

Figure S1 Comparison of with and without cropping for RBC speed estimation. (A) Raw image (512 by 512 pixels) captured by line scanning along a single vessel. The regions of interest in blue (cropped,128 by 128 pixels) and pink (non cropped, 512 by 128 pixels) were compared. (B) FFT. A single peak was consistently seen for both the cropped (blue) and non-cropped (pink) images. (C) Radon transform. Identical peak location was observed for the cropped (blue) and non-cropped (pink) images, but in the latter case the peak height was hidden by the components originating from non-vascular areas of the non-cropped image.
(PDF)

Figure S2 Temporal window and estimated RBC speeds. The dependence of RBC speed estimation on temporal window size was compared for the FFT and Radon transform methods. For less than 32 pixels (x-axis), both methods produced large variations away from the expected velocities (1 mm/s). Thus, a minimum of 32 pixels was needed to achieve accurate estimation. Note that the time window dependencies were similar for both the FFT and Radon transform methods.
(PDF)

Figure S3 RBC speed histogram for the non-exposed animals (modified from [30]). The RBC speed was directly measured by tracking the displacement of individual RBCs in the non-exposed rats [30] under similar experimental conditions to the present study. A mean speed of 1.5±0.4 mm/s was observed.
(PDF)

Acknowledgments

The authors thank Dr. Jeffrey Kershaw for proof reading.

Author Contributions

Conceived and designed the experiments: JA HK IA TO KM IK. Performed the experiments: JA HK SS KM. Analyzed the data: JA HK KM. Contributed reagents/materials/analysis tools: SS IA TO KM. Wrote the paper: JA HK KM IK.

References

1. Kimler BF (1998) Prenatal irradiation: a major concern for the developing brain. Int J Radiat Biol 73: 423–434.
2. Saito S, Aoki I, Sawada K, Sun XZ, Chuang KH, et al. (2011) Quantitative and noninvasive assessment of prenatal X-ray-induced CNS abnormalities using magnetic resonance imaging. Radiat Res 175: 1–9.
3. Ma YP, Koo A, Kwan HC, Cheng KK (1974) On-line measurement of the dynamic velocity of erythrocytes in the cerebral microvessels in the rat. Microvasc Res 8: 1–13.
4. Villringer A, Them A, Lindauer U, Einhäupl K, Dirnagl U (1994) Capillary perfusion of the rat brain cortex. An in vivo confocal microscopy study. Circ Res 75: 55–62.
5. Hudetz AG, Fehér G, Weigle CG, Knuese DE, Kampine JP (1995) Video microscopy of cerebrocortical capillary flow: response to hypotension and intracranial hypertension. Am J Physiol 268: H2202–H2210.
6. Seylaz J, Charbonné R, Nanri K, Von Euw D, Borredon J, et al. (1999) Dynamic in vivo measurement of erythrocyte velocity and flow in capillaries and of microvessel diameter in the rat brain by confocal laser microscopy. J Cereb Blood Flow Metab 19: 863–870.
7. Schulte ML, Wood JD, Hudetz AG (2003) Cortical electrical stimulation alters erythrocyte perfusion pattern in the cerebral capillary network of the rat. Brain Res 963: 81–92.
8. Kleinfeld D, Mitra PP, Helmchen F, Denk W (1998) Fluctuations and stimulus-induced changes in blood flow observed in individual capillaries in layers 2 through 4 of rat neocortex. Proc Natl Acad Sci U S A 95: 15741–15746.
9. Denk W, Strickler JH, Webb WW (1990) Two-photon laser scanning fluorescence microscopy. Science 248: 73–76.
10. Helmchen F, Denk W (2005) Deep tissue two-photon microscopy. Nat Methods 2: 932–940.
11. Kobat D, Durst ME, Nishimura N, Wong AW, Schaffer CB, et al. (2009) Deep tissue multiphoton microscopy using longer wavelength excitation. Opt Express 17: 13354–13364.
12. Dunn AK, Wallace VP, Coleno M, Berns MW, Tromberg BJ (2000) Influence of optical properties on two-photon fluorescence imaging in turbid samples. Appl Opt 39: 1194–1201.
13. Ying J, Liu F, Alfano RR (2000) Effect of scattering on nonlinear optical scanning microscopy imaging of highly scattering media. Appl Opt 39: 509–514.
14. Drew PJ, Blinder P, Cauwenberghs G, Shih AY, Kleinfeld D (2010) Rapid determination of particle velocity from space-time images using the Radon transform. J Comput Neurosci 29: 5–11.
15. Rovainen CM, Woolsey TA, Blocher NC, Wang DB, Robinson OF (1993) Blood flow in single surface arterioles and venules on the mouse somatosensory cortex measured with videomicroscopy, fluorescent dextrans, nonoccluding fluorescent beads, and computer-assisted image analysis. J Cereb Blood Flow Metab 13: 359–371.
16. Beck J, Stummer W, Lehmberg J, Baethmann A, Uhl E (2007) Arteriovenous transit time as a measure for microvascular perfusion in cerebral ischemia and reperfusion. Neurosurgery 61: 826–833.
17. Ellis CG, Ellsworth ML, Pittman RN, Burgess WL (1992) Application of image analysis for evaluation of red blood cell dynamics in capillaries. Microvasc Res 44: 214–225.
18. Schaffer CB, Friedman B, Nishimura N, Schroeder LF, Tsai PS, et al. (2006) Two-photon imaging of cortical surface microvessels reveals a robust redistribution in blood flow after vascular occlusion. PLoS Biol 4: e22.
19. Zipfel WR, Williams RM, Webb WW (2003) Nonlinear magic: multiphoton microscopy in the biosciences. Nat Biotechnol 21: 1369–1377.

20. Dobbe JG, Streekstra GJ, Atasever B, van Zijderveld R, Ince C (2008) Measurement of functional microcirculatory geometry and velocity distributions using automated image analysis. Med Biol Eng Comput 46: 659–670.
21. Duncan DD, Lemaillet P, Ibrahim M, Nguyen QD, Hiller M, et al. (2010) Absolute blood velocity measured with a modified fundus camera. J Biomed Opt 15: 056014.
22. Stefanovic B, Hutchinson E, Yakovleva V, Schram V, Russell JT, et al. (2008) Functional reactivity of cerebral capillaries. J Cereb Blood Flow Metab 28: 961–972.
23. Petzold GC, Albeanu DF, Sato TF, Murthy VN (2008) Coupling of neural activity to blood flow in olfactory glomeruli is mediated by astrocytic pathways. Neuron 58: 897–910.
24. Drew PJ, Shih AY, Driscoll JD, Knutsen PM, Blinder P, et al. (2010) Chronic optical access through a polished and reinforced thinned skull. Nat Methods 7: 981–984.
25. Hirase H, Creso J, Buzsáki G (2004) Capillary level imaging of local cerebral blood flow in bicuculline-induced epileptic foci. Neuroscience 128: 209–216.
26. Zhang S, Boyd J, Delaney K, Murphy TH (2005) Rapid reversible changes in dendritic spine structure in vivo gated by the degree of ischemia. J Neurosci 25: 5333–5338.
27. Chaigneau E, Oheim M, Audinat E, Charpak S (2003) Two-photon imaging of capillary blood flow in olfactory bulb glomeruli. Proc Natl Acad Sci U S A 100: 13081–13086.
28. Japee SA, Pittman RN, Ellis CG (2005) Automated method for tracking individual red blood cells within capillaries to compute velocity and oxygen saturation. Microcirculation 12: 507–515.
29. Malone MH, Sciaky N, Stalheim L, Hahn KM, Linney E, et al. (2007) Laser-scanning velocimetry: a confocal microscopy method for quantitative measurement of cardiovascular performance in zebrafish embryos and larvae. BMC Biotechnol 7: 40.
30. Masamoto K, Obata T, Kanno I (2010) Intracortical microcirculatory change induced by anesthesia in rat somatosensory cortex. Adv Exp Med Biol 662: 57–61.
31. Hutchinson EB, Stefanovic B, Koretsky AP, Silva AC (2006) Spatial flow-volume dissociation of the cerebral microcirculatory response to mild hypercapnia. Neuroimage 32: 520–530.
32. Hendrich KS, Kochanek PM, Melick JA, Schiding JK, Statler KD, et al. (2001) Cerebral perfusion during anesthesia with fentanyl, isoflurane, or pentobarbital in normal rats studied by arterial spin-labeled MRI. Magn Reson Med 46: 202–206.
33. Masamoto K, Kim T, Fukuda M, Wang P, Kim SG (2007) Relationship between neural, vascular, and BOLD signals in isoflurane-anesthetized rat somatosensory cortex. Cereb Cortex 17: 942–950.
34. Maekawa T, Tommasino C, Shapiro HM, Keifer-Goodman J, Kohlenberger RW (1986) Local cerebral blood flow and glucose utilization during isoflurane anesthesia in the rat. Anesthesiology 65: 144–151.
35. Hudetz AG, Lee JG, Smith JJ, Bosnjak ZJ, Kampine JP (1994) Effects of volatile anesthetics on cerebrocortical laser Doppler flow: hyperemia, autoregulation, carbon dioxide response, flow oscillations, and role of nitric oxide. Adv Pharmacol 31: 577–593.
36. Tomita M, Osada T, Schiszler I, Tomita Y, Unekawa M, et al. (2008) Automated method for tracking vast numbers of FITC-labeled RBCs in microvessels of rat brain in vivo using a high-speed confocal microscope system. Microcirculation 15: 163–174.
37. Unekawa M, Tomita M, Tomita Y, Toriumi H, Miyaki K, Suzuki N (2010) RBC velocities in single capillaries of mouse and rat brains are the same, despite 10-fold difference in body size. Brain Res 1320: 69–73.
38. Schiszler I, Tomita M, Fukuuchi Y, Tanahashi N, Inouc K (2000) New optical method for analyzing cortical blood flow heterogeneity in small animals: validation of the method. Am J Physiol Heart Circ Physiol 279: H1291–H1298.
39. Tomita Y, Tomita M, Schiszler I, Amano T, Tanahashi N, et al. (2002) Moment analysis of microflow histogram in focal ischemic lesion to evaluate microvascular derangement after small pial arterial occlusion in rats. J Cereb Blood Flow Metab 22: 663–669.
40. Tomita Y, Pinard E, Tran-Dinh A, Schiszler I, Kubis N, et al. (2011) Long-term, repeated measurements of mouse cortical microflow at the same region of interest with high spatial resolution. Brain Res 1372: 59–69.
41. Rubin P, Gash DM, Hansen JT, Nelson DF, Williams JP (1994) Disruption of the blood-brain barrier as the primary effect of CNS irradiation. Radiother Oncol 31: 51–60.
42. Ljubimova NV, Levitman MK, Plotnikova ED, Eidus LKh (1991) Endothelial cell population dynamics in rat brain after local irradiation. Br J Radiol 64: 934–940.
43. Peña LA, Fuks Z, Kolesnick RN (2000) Radiation-induced apoptosis of endothelial cells in the murine central nervous system: protection by fibroblast growth factor and sphingomyelinase deficiency. Cancer Res 60: 321–327.
44. Baker DG, Krochak RJ (1989) The response of the microvascular system to radiation: a review. Cancer Invest 7: 287–294.
45. Miki T, Fukui Y, Takeuchi Y, Itoh M (1995) A quantitative study of the effects of prenatal X-irradiation on the development of cerebral cortex in rats. Neurosci Res 23: 241–247.
46. Miki T, Yokoyama T, Sumitani K, Wang ZY, Yang W, et al. (2007) The effect of prenatal X-irradiation on the developing cerebral cortex of rats. II: A quantitative assessment of glial cells in the somatosensory cortex. Int J Dev Neurosci 25: 293–297.

NeuroImage 57 (2011) 140–148

Contents lists available at ScienceDirect

NeuroImage

journal homepage: www.elsevier.com/locate/ynimg

High *b*-value diffusion-weighted fMRI in a rat forepaw electrostimulation model at 7 T

Joonas A.A. Autio [a,b], Jeff Kershaw [a,c,*], Sayaka Shibata [a], Takayuki Obata [a], Iwao Kanno [a], Ichio Aoki [a]

[a] Molecular Imaging Centre, National Institute of Radiological Sciences, Chiba 263-8555, Japan
[b] Department of Neurobiology, A. I. Virtanen Institute for Molecular Sciences, University of Eastern Finland, PO Box 1627, 70211 Kuopio, Finland
[c] School of Bioscience and Biotechnology, Tokyo Institute of Technology, Yokohama 226-8503, Japan

ARTICLE INFO

Article history:
Received 1 October 2010
Revised 15 March 2011
Accepted 2 April 2011
Available online 12 April 2011

Keywords:
Diffusion-weighted functional MRI
Spin-echo BOLD
USPIO
Rat
Somatosensory cortex

ABSTRACT

Spin-echo diffusion-weighted functional MRI (DW-fMRI) was performed on a rat forepaw electrostimulation model at 7 T. This small animal model used electric (rather than visual) stimulation and allowed DW-fMRI experiments to be performed over a broader range of acquisition parameters than previous work on humans and cats. Resting state experiments with injections of ultra-small superparamagnetic iron oxide (USPIO) were also used to investigate the effects of gradient coupling on the signal change. The experiments were performed over five *b*-values (0, 200, 800, 1400 and 2000 s/mm^2) and three echo-times (30, 60 and 90 ms). Alterations to the stimulation-induced response with respect to TE and *b*-value were evaluated in two intervals: the positive stimulus-correlated response (5–20 s after stimulus onset) and the post-stimulus undershoot (27–40 s). There was no strong dependence of the signal change on *b*-value for any of the intervals or TEs. Similarly, changes to the apparent transverse relaxation rate showed no clear dependence on *b*-value. In contrast to previous DW-fMRI studies, the simplest explanation for the observed data is a single-compartment signal model with the functional signal changes probably corresponding to extravascular SE-BOLD. Experiments with USPIO suggested that at 7 T and within the range of parameters used, the influence of gradient coupling may be sufficient to explain minor DW-fMRI signal changes.

Introduction

Over the past few years, diffusion-weighted functional MRI (DW-fMRI) has attracted attention as a technique that might provide information more directly correlated with the actual neural activity than standard blood oxygen-level dependent (BOLD) fMRI (Darquie et al., 2001; Le Bihan et al., 2006; Gangstead and Song, 2002; Song et al., 2002; Harshbarger and Song, 2006). When motion-probing gradients (MPGs) were applied during fMRI experiments, the amplitude and onset of the response were found to be dependent on the diffusion-weighting, as characterised by the *b*-value. Although there were differences in the experimental setup (through factors such as the type of animal, field strength and stimulus paradigm) and the imaging protocol (via imaging sequence and range of acquisition parameters), changes to the response amplitude in most previous DW-fMRI studies were roughly consistent with a signal decrease for *b*-values in the range 0–600 s/mm^2, followed by an increase for higher *b*-values up to 2400 s/mm^2 (Le Bihan et al., 2006; Miller et al., 2007; Jin et al., 2006b; Yacoub et al., 2008; Kershaw et al., 2009; Kuroiwa et al., 2009). For *b*-values 0–600 s/mm^2, the signal changes have been largely attributed to attenuation of the blood contribution (Jochimsen et al., 2004; Duong et al., 2003; Le Bihan et al., 1998; Callaghan, 1991).

To date, all explanations put forward for high *b*-value DW-fMRI signal changes have been based on some form of compartmentalisation of in vivo water signal. A common feature of these models is the assumption that the diffusion coefficient of each compartment remains unchanged by the application of the stimulus. That is, rather than invoking real changes to the diffusion properties of water, the signal changes are explained as a mixture of competing changes to compartmental volume fractions or transverse relaxation rates. In the paper of Le Bihan et al. (2006), it was proposed that the effects observed at high *b*-value are the result of extravascular (EV) water molecules transferring between slow- and fast-diffusion phases

Abbreviations: fMRI, functional magnetic resonance imaging; DW-fMRI, diffusion-weighted fMRI; BOLD, blood oxygen-level dependent; MPG, motion-probing gradient; ADC, apparent diffusion coefficient; IV, intravascular; EV, extravascular; CSF, cerebro-spinal fluid; TE, echo-time; SE, spin echo; EPI, echo-planar imaging; ROI, region-of-interest; PSCR, positive stimulus-correlated response; PSU, post-stimulus undershoot; USPIO, ultra-small superparamagnetic iron-oxide.

* Corresponding author at: Molecular Imaging Centre, National Institute of Radiological Sciences, 4-9-1 Anagawa, Inage-ku, Chiba 263-8555 Japan. Fax: +81 43 206 0819.
E-mail address: len@nirs.go.jp (J. Kershaw).

1053-8119/$ – see front matter © 2011 Elsevier Inc. All rights reserved.
doi:10.1016/j.neuroimage.2011.04.006

during stimulus-induced cell swelling. This model was later modified to include residual intravascular (IV) components and to take into account possible changes to the apparent transverse relaxation rate of tissue (Aso et al., 2009). Kershaw et al. (2009) also used an extravascular compartmentalisation into slow and fast diffusing water molecules, but in this case it was suggested that alteration of the DW-fMRI signal is due to distinct changes to the transverse relaxation rates of each compartment. Harshbarger and Song (2006) suggested an interpretation based on an IV–EV separation of signal that increasingly reflects cerebral-blood-volume-weighting at higher *b*-values. In a series of papers, Jin et al. put forward a picture dividing the signal into tissue, arterial blood, venous blood and cerebrospinal-fluid (CSF) compartments (Jin et al., 2006a,b; Jin and Kim, 2008). From their experiments on domestic cats at 9.4 T, they essentially argued that no new mechanism is required to explain changes to the apparent diffusion coefficient (ADC) during high *b*-value DW-fMRI because the observations could be attributed to changes in one or other of those compartments.

Another factor that has been mentioned as a possible source of DW-fMRI signal changes is the so-called "coupling" of the applied MPGs and internal field inhomogeneities (Jin and Kim, 2008; Miller et al., 2007; Yacoub et al., 2008; Pampel et al., 2010). It has long been known that the presence of subvoxel susceptibility variations can affect diffusion measurements (Stesjkal and Tanner, 1965; Zhong et al., 1991, 1998). It is also recognised that the BOLD effect, which is related to the diffusion of water molecules through the field gradients within and surrounding blood vessels, may be perturbed by the applied MPGs so that a significant dependence on *b*-value may be observable. However, simulations performed by Pampel et al. (2010) found that superposition of applied MPGs and blood-vessel-induced field gradients would most likely reduce, rather than increase, the fractional signal change with increasing *b*-value. It was therefore concluded that this mechanism is unlikely to be responsible for the DW-fMRI signal increases observed at high *b*-value, but may instead obscure other sources of signal change.

In principle, an explanation for DW-fMRI signal changes should apply to other stimulus types, brain-sensory systems and animal models. Previous high *b*-value DW-fMRI studies have been limited to visual stimulation on either humans or domestic cats. Visual stimulation is a reliable technique that elicits a physiological response that is detectable with fMRI. However, it is not yet known whether the signal changes observed with high *b*-value DW-fMRI also translate to other functional imaging models. Another constraint of previous work is the limited number of experiments that can be performed on human subjects, which restricts the range of imaging parameters that can be used in each study. Experiments on cats are less constrained by this problem, yet the range of parameters used in previous studies has been limited. Performing experiments over a broader range of TEs and *b*-values may help to distinguish between different interpretations.

A model widely used in functional MR imaging research is the rat forepaw electrostimulation model. The functional response in this small animal model has been extensively studied for the $b=0$ case (e.g. Keilholz et al. (2006); Kennan et al. (1998); Lee et al. (2002); Mandeville and Marota (1999)). However, even though there have been experiments with applied MPGs of up to 500 s/mm^2 at 9.4 T (Lee et al., 1999), there have been no high *b*-value studies. An advantage of the rat forepaw model is that longer experiments can be performed, allowing DW-fMRI signal changes to be investigated over a broader range of acquisition parameters. This model also uses electric stimulation to activate the somatosensory cortex, so that both the stimulus type and brain-sensory system differ from previous work. The present manuscript reports the results of spin-echo echo-planar imaging (SE-EPI) DW-fMRI experiments performed at 7 T with the rat forepaw electrostimulation model. The response was measured for *b*-values 0–2000 s/mm^2 and TEs 30–90 ms.

Theoretical background

The baseline signal from a multicompartmental system in slow exchange can be written as

$$S = \sum_i S_{oi} e^{-bD_i} e^{-\mathrm{TE}R_{2ai}}, \tag{1}$$

where D_i and R_{2ai} are the apparent diffusion coefficient and apparent transverse relaxation rate of compartment i, respectively. S_{oi} is an aggregation of quantities like the compartmental volume fraction and proton density, but is essentially the compartmental signal intensity when b and TE are zero. Following previous models of high *b*-value DW-fMRI signal changes in assuming that physiological changes during stimulation only affect the S_{oi} and R_{2ai}, it ensues that the fractional signal change is

$$\frac{\Delta S}{S} = \frac{\sum_i (S_{oi} + \Delta S_{oi}) e^{-bD_i}\ e^{-\mathrm{TE}(R_{2ai} + \Delta R_{2ai})}}{\sum_i S_{oi}\ e^{-bD_i}\ e^{-\mathrm{TE}R_{2ai}}} - 1. \tag{2}$$

For the special case of one compartment, the logarithmic fractional signal change

$$\ln\left(1 + \frac{\Delta S}{S}\right) = \ln\left(1 + \frac{\Delta S_o}{S_o}\right) - \mathrm{TE}\Delta R_{2a} \tag{3}$$

is linear in TE and independent of *b*-value. After some algebraic manipulation, the expression for two or more compartments is

$$\begin{aligned} \ln\left(1 + \frac{\Delta S}{S}\right) &= \ln\left(1 + \frac{\Delta S_{oj}}{S_{oj}}\right) - \mathrm{TE}\Delta R_{2aj} \\ &\quad + \ln\left(\frac{1 + \sum_{i\neq j} B_i(b,\mathrm{TE}) F_i(b,\mathrm{TE})}{1 + \sum_{i\neq j} B_i(b,\mathrm{TE})}\right), \\ B_i(b,\mathrm{TE}) &= \left(\frac{S_{oi}}{S_{oj}}\right) e^{-b(D_i - D_j) - \mathrm{TE}(R_{2ai} - R_{2aj})}, \\ F_i(b,\mathrm{TE}) &= \left(\frac{1 + \Delta S_{oi}/S_{oi}}{1 + \Delta S_{oj}/S_{oj}}\right) e^{-\mathrm{TE}(\Delta R_{2ai} - \Delta R_{2aj})}. \end{aligned} \tag{4}$$

Note that the last term on the right-hand side of Eq. (4) is a nonlinear function of b, TE and the compartmental parameters.

To fit experimental data to a nonlinear function it is usually necessary to use an iterative nonlinear fitting algorithm. It is well known that the success of this procedure depends on the quality of the data, as even small uncertainties in the data can lead to unreasonably large uncertainty in the parameter estimates, in particular for the rate constants. Instead of directly fitting the data to a multicompartmental model, an alternative strategy that has been used when interpreting DW-fMRI data is to select a range of physiologically relevant values for the parameters, simulate the expected signal changes with the model, and then compare the empirical measurements to the simulations (e.g. Duong et al.,2003; Jin et al.,2006a,b). However, that approach is based on specific models where the number of compartments is chosen a priori. In the procedure adopted for this work, no a priori selection of the model form is made. Rather, the simple signal model $S = S_o\, e^{-bADC} e^{-TER_{2a}}$ is used, from which it follows that

$$\ln\left(1 + \frac{\Delta S}{S}\right) = \ln\left(1 + \frac{\Delta S_o}{S_o}\right) - \mathrm{TE}\ \Delta R_{2a} - b\ \Delta ADC. \tag{5}$$

The similarity between this equation and Eq. (4) is immediate if a correspondence between ΔADC and the nonlinear term on the right-hand side of Eq. (4) is made. The advantages of Eq. (5) are that the fitting procedure is linear and the experimental results across a

relatively wide range of acquisition parameters can be summarised by the small number of model parameters. The strategy is to fit the data to Eq. (5) over either b or TE and then observe the dependence of the parameter estimates on the other independent variable. In the simplest case where the signal originates from a single compartment, ΔADC will be zero and the results can be described by Eq. (3). In contrast, if two or more compartments are contributing to the signal in a manner consistent with any of the existing interpretations for high b-value DW-fMRI, the ΔADC will be nonzero and the dependence on b and TE can help to identify the number of signal compartments.

Materials and methods

All experiments were approved by the Animal Welfare Committee of the National Institute of Radiological Sciences, Chiba City, Japan.

DW-fMRI experiments

Male Sprague–Dawley rats (258 ± 23 g, (220–302 g), n = 15) were initially anesthetised with 4% isoflurane via a calibrated vaporiser with a mixture of O_2 (27–33%) and N_2O (73–67%). Intubation was performed for mechanical ventilation, and a catheter was inserted into the femoral artery for arterial blood-pressure monitoring and blood-gas sampling. The animal was fixed in a cradle with bite and ear bars. Needle electrodes were inserted under the skin between digits 2 and 3 and digits 4 and 5 of the left forepaw. The cradle was placed in the bore of the magnet and then rotated so that the animal was lying on its back to minimise artefacts due to respiratory motion. After finalising animal, coil and cradle positioning, the anaesthesia was switched to α-chloralose with an initial bolus of 60 mg/kg followed by hourly injections of 40 mg/kg. The respiration rate and volume were adjusted so that the blood gas and physiology readings were within normal bounds before beginning the functional experiments. Rectal temperature was maintained at around 37 °C with heated air.

All MRI data were acquired on a 7 T MRI system (Magnet: Kobelco, Japan; Console: Bruker Avance I, Germany) equipped with an actively-screened gradient system (Bruker BGA12), in combination with a volume coil (diameter 72 mm, Bruker) for transmission and a 2-channel phased-array surface coil (Rapid Biomedical, Germany) for signal reception. Gradient-echo scout images were acquired to identify a transaxial slice through the somatosensory cortex. All fMRI data were obtained using a single-shot single-SE-EPI sequence with Stejskal-Tanner-type MPGs placed on either side of the π-refocusing pulse. Experiments on each animal were performed such that a single TE (either 30, 60 or 90 ms) was selected, and then images with b-values of 0, 200, 800, 1400 (×2) and 2000 (×3) s/mm^2 were acquired with MPG separation (Δ) 15 ms and MPG duration (δ) 5 ms. Runs were performed twice on each animal for the $b = 1400$ s/mm^2 and three times for the $b = 2000$ s/mm^2 experiments to improve the signal-to-noise ratio. The order of experiments was randomised. Other imaging parameters were: FOV = 25 mm × 25 mm, slice thickness = 2 mm, number of slices = 3 (with an interslice gap of 0.5 mm), matrix size = 64 × 64 and repetition time TR = 2 s. Additional experiments at a TE of 20 ms were performed on five of the animals. In this case Δ and δ were 9.5 and 2 ms, respectively, and the maximum b-value was restricted to 200 s/mm^2.

Electric stimulation was provided by a programmable stimulus generator (STG2004, Multi Channel Systems, Germany), and consisted of square pulses (width 0.3 ms and amplitude 2.0 mA) applied at a frequency of 3 Hz. For each run, the stimulus paradigm consisted of 60 s of rest followed by blocks of [20 s stimulation + 100 s rest] repeated 5 times. The long 100 s rest period was chosen to ensure that the response had returned to baseline before the next stimulus period began.

Acquired data were reconstructed and analysed using purpose-written Matlab code (The MathWorks Inc., Natick, MA, USA). No spatial or temporal smoothing was applied at any point of the analysis. Using either the 30 or 60 ms TE data, activated pixels were identified with an algorithm based on Bayesian probability analysis (Kershaw et al., 1999). Briefly, the time-series at each pixel was compared to a boxcar-like test function representing the stimulus on–off periods and the probability that the pixel contains activation was calculated. A pixel was considered to contain significant activation if it had a probability greater than 0.99 (equivalent to a significance of less than 0.01). To minimise the possibility of including pixels that have a significant response only because they contain large veins downstream from the main activation site, regions-of-interest (ROIs) containing activated pixels in and around the somatosensory cortex were selected from both the $b = 200$ and 800 s/mm^2 activation maps of each subject (see Figs. 1a and b). The intersection of the two ROIs was then placed on the ADC map calculated from the $b = 0$–800 s/mm^2 images and pixels near the brain surface were trimmed to avoid a potentially large CSF contribution (Fig. 1c).

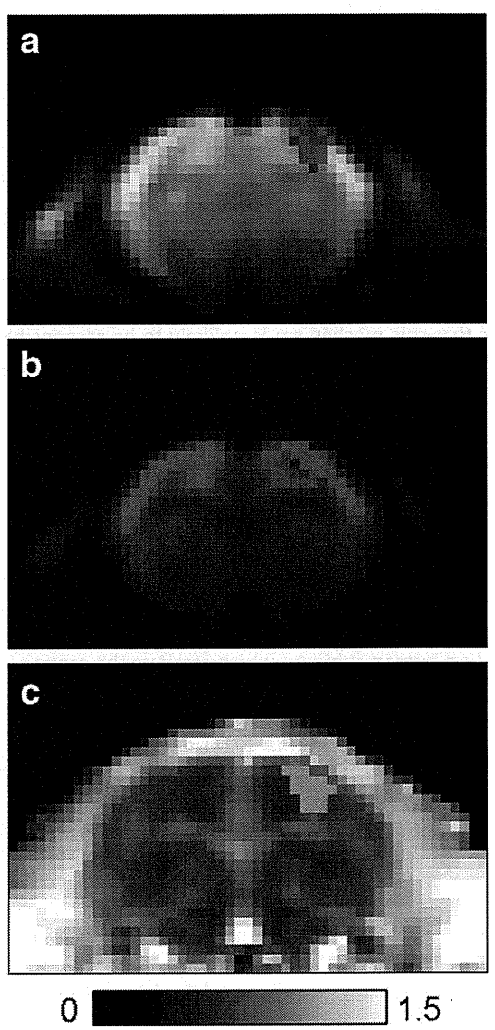

Fig. 1. Typical activation maps calculated from DW-fMRI data acquired with b-values of (a) 200, and (b) 800 s/mm^2. The maps are overlaid on the mean of the SE-EPI images acquired during the initial 60 s rest period. The location of the activation centre consistently coincided with the contralateral somatosensory cortex. (c) Pixels selected for the final trimmed intersection-ROI are shown in green, whilst the pixels in red were excluded for the reasons described in the DW-fMRI experiments section. The ADC map in the background shows the proximity of the red pixels to either the white matter of the corpus callosum and external capsule, or areas near the surface with a potentially large CSF contribution. The greyscale bar represents the ADC in units of $\times 10^{-3}$ mm^{2}s^{-1}.

Similarly, pixels near the corpus callosum and external capsule were rejected so as to avoid possible partial-voluming with white matter. The pixels in the final trimmed intersection-ROI were used for further analysis of all data from the same animal. The baseline-level of the time-course at each ROI pixel was estimated by performing a least-squares fit of a straight line to the data points within intervals where it was expected that no response would be present (first 0–58 s of each scan plus the periods 100–118 s after each stimulus onset; see Fig. 2b). Normalised DW-fMRI time-courses ($\Delta S/S$) were obtained for each experiment by subtracting and then dividing by the baseline-level, before averaging across ROI pixels and cycles.

For each experiment, changes to the shape of the response with respect to either TE or b were evaluated by calculating the mean signal change of points in two selected intervals illustrated in Fig. 2a: the positive stimulus-correlated response (PSCR) (5–20 s after stimulus onset, encompassing 8 images) and the post-stimulus undershoot (PSU) (27–40 s, 7 images). Estimates of the unknown parameters were obtained with linear least-squares when fits to the data were performed. Uncertainty in the parameter estimates was evaluated by bootstrapping the original data set (Efron and Tibshirani, 1994).

USPIO experiments

An empirical estimate of the effect of coupling between applied and internal gradients on DW-fMRI signal changes at 7 T was obtained by following a procedure similar to that first used by Does et al. (1999) at 2 T and later by Jin and Kim (2008) at 9.4 T. Briefly, resting-state diffusion-weighted measurements were performed on rats whilst artificially altering the IV–EV susceptibility difference with injections of an IV contrast agent (ultra-small superparamagnetic iron oxide (USPIO), Molday ION, BioPAL, USA). The animals were prepared and placed in the scanner in the same way that the functional studies were performed. Using the same SE-EPI sequence and slice orientations, images were then acquired over the same range of b-values and TEs as for the functional images. After each image series, an injection of USPIO (volume 100 μl, concentration 10 mg Fe/ml) was given to the animal through an intravenous catheter and the imaging procedure was repeated. The data was fitted to Eq. (5) to obtain estimates of ΔR_{2a} and ΔADC at each USPIO concentration.

Results

Animal physiology during the experiments was characterised by the following readings: blood pressure = 94.4 ± 18.6 mm Hg, heart rate = 373 ± 59 bpm, $PaCO_2$ = 41.4 ± 4.8 mm Hg, pH = 7.36 ± 0.03, and PaO_2 = 126 ± 21 mm Hg.

Activation maps from the DW-fMRI experiments consistently showed clear functional response in the contralateral somatosensory cortex and the location of the activation centre was similar for the b = 200 and 800 data as well as across TEs. A typical example is shown in Fig. 1. Figs. 2a–c present the mean b = 0 time-courses (black lines) for TEs 30–90 ms. Regardless of TE, the responses are qualitatively similar as they all have well-defined PSCRs and clear PSUs before returning to the baseline level. Also plotted on the same axes are the corresponding mean b = 2000 time-courses (light grey lines), the characteristics of which are similar to the b = 0 curves.

The dependence of the b = 0 and 2000 responses on TE is illustrated in Fig. 2d for the PSCR and PSU intervals. Fits to the data with Eq. (5) over the TE range 30–90 ms are also plotted for the two b-values. Similar fits were also performed for the other b-values and

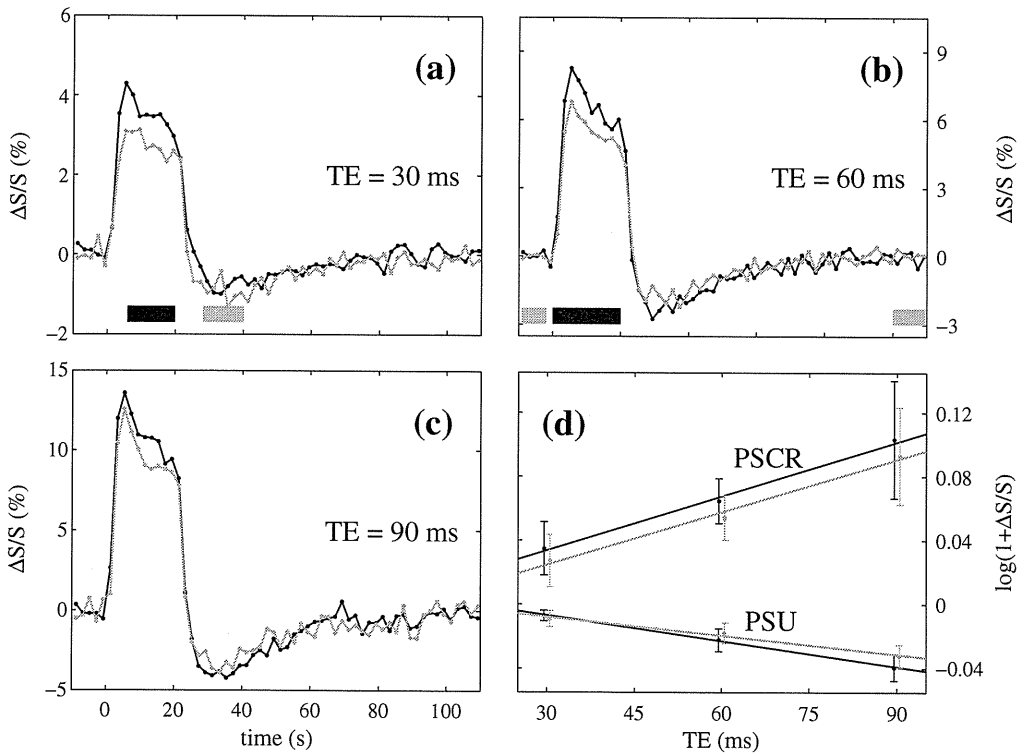

Fig. 2. Mean b = 0 (black) and b = 2000 (light grey) time-courses for (a) TE = 30 ms, (b) TE = 60 ms, and (c) TE = 90 ms. The bars in (a) represent the extent of the PSCR (black) and PSU (light grey) analysis intervals. The bars in (b) indicate the stimulus period (black) and the interval used to determine the baseline of the functional responses (light grey). Note that the horizontal scales of parts (a) and (b) are the same as that in (c). (d) $ln(1 + \Delta S/S)$ for each of the analysis intervals plotted as a function of TE. The b = 0 (black) and b = 2000 (light grey) curves are offset slightly by −0.5 and 0.5 ms, respectively, so that the standard deviation across subjects can be plotted without overlap. The lines are fits to Eq. (5) as a function of TE.

Table 1
Estimates of ΔR_{2a} as a function of b-value (above), and estimates of ΔADC as a function of TE (below) for each of the analysis intervals. The estimates obtained after pooling the data over all TEs and b-values are denoted by *All*. Data are presented as estimate ± s.d. (95% confidence interval) {R^2}, where R^2 is the coefficient of determination of the fit.

	PSCR	PSU
b (s/mm^2)	ΔR_{2a} (s^{-1})	
0	−1.13 ± 0.24(−1.52, −0.57) {0.79}	0.49 ± 0.04(0.42, 0.56) {0.93}
200	−1.26 ± 0.19(−1.60, −0.86) {0.86}	0.44 ± 0.07(0.28, 0.56) {0.82}
800	−1.19 ± 0.21(−1.55, −0.73) {0.82}	0.38 ± 0.03(0.33, 0.44) {0.92}
1400	−1.19 ± 0.21(−1.56, −0.71) {0.81}	0.41 ± 0.05(0.28, 0.50) {0.82}
2000	−1.10 ± 0.23(−1.45, −0.51) {0.79}	0.39 ± 0.06(0.25, 0.49) {0.84}
All	−1.18 ± 0.09(−1.35, −0.98) {0.82}	0.42 ± 0.02(0.38, 0.47) {0.86}
TE (ms)	ΔADC (× 10^{-6} mm^2 s^{-1})	
30	3.99 ± 3.52(−3.39, 10.60) {0.19}	0.40 ± 0.94(−1.28, 2.37) {0.07}
60	4.89 ± 3.36(−1.85, 11.15) {0.22}	−2.82 ± 1.64(−5.96, 0.50) {0.28}
90	6.50 ± 7.28(−7.32, 21.26) {0.17}	−2.92 ± 1.97(−7.01, 0.73) {0.27}
All	5.36 ± 2.78(−0.10, 10.87)	−1.77 ± 0.90(−3.56, −0.04)

the resulting ΔR_{2a} estimates are presented in Table 1. The coefficient of determination (R^2) of each fit signified that the logarithmic fractional signal change was well described by Eq. (5), with the linear relationship accounting for 79–93% of the variation in the data. Also, the substantial overlap of the 95% confidence intervals indicates that the ΔR_{2a} estimates are not strongly influenced by the b-value over the range 0–2000 s/mm^2.

Fig. 3 presents the signal change during the PSCR and PSU intervals as a function of b-value at TEs of 30, 60 and 90 ms. Inspection finds that there is no strong dependence of the signal change on b-value for any of the intervals. However, the mean behaviour of the PSCR and PSU interval data suggests a gradual decrease and increase, respectively, of the signal amplitude with increasing b-value. The signal changes were characterised for each TE by estimates of ΔADC obtained from fitting Eq. (5) to the data as a function of b-value. Fig. 4 (black bars) displays the results for the two selected intervals (see also Table 1). The R^2 values obtained from the fits show that less than 30% of the variance in the logarithmic signal change can be explained by correlation with the b-value. Moreover, the 95% confidence bounds demonstrate no strong evidence that ΔADC is significantly different from zero over the range 30–90 ms for either of the analysis intervals. Since neither ΔADC nor ΔR_{2a} displayed any strong dependence on b-value, the data was again fitted to Eq. (5) after pooling across TEs. The increase in the number of data points has reduced the uncertainty without substantially altering the estimates of ΔADC and ΔR_{2a} (Fig. 4 (grey bars); see also Table 1).

The $b=0$ and 200 time-courses from the TE 20 ms experiments are presented in Fig. 5a. Both time-courses demonstrate the same qualitative behaviour as the longer TE responses in Figs. 2a–c. Fig. 5b compares the PSCR and PSU between $b=0$ and $b=200$ for all TEs. Paired-t tests found no significant differences for the TE 30–90 ms data. However, there was a weakly significant difference ($p=0.058<0.1$) for the PSCR of the TE 20 ms data.

The results plotted in Fig. 6 for the USPIO experiments demonstrate that changes to the ADC due to the iron-oxide particles in the vasculature are linearly correlated with changes in R_{2a}, which is consistent with the results obtained at 2 T (Does et al., 1999) and 9.4 T (Jin and Kim, 2008). The straight line fitted to the data has the form $\Delta ADC = (-6.01 \pm 0.31) \times 10^{-6}\ \Delta R_{2a} + (2.5 \pm 5.2) \times 10^{-6}$. Before USPIO injection, the ADC was estimated to be $[563 \pm 8(548, 579)] \times 10^{-6}$ mm^{2}s^{-1}. Also plotted in Fig. 6 are the (ΔR_{2a}, ΔADC) pairs estimated for the PSCR (blue) and PSU (red) after pooling the functional data.

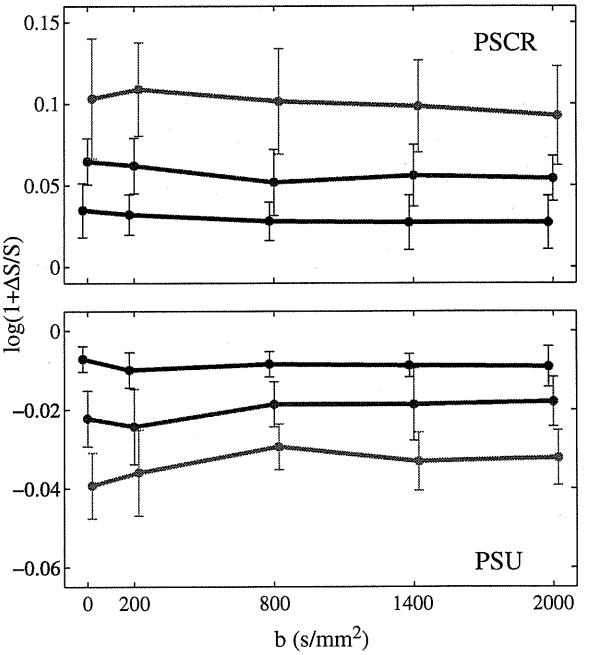

Fig. 3. $ln(1+\Delta S/S)$ as a function of b-value at TEs of 30 (blue), 60 (green), and 90 ms (red) during the PSCR (upper) and PSU (lower) intervals. The error bars indicate the standard deviation across subjects. The blue and red curves are offset slightly by −20 and 20 s/mm^2, respectively, so that the standard deviation can be plotted without overlapping with those of the other curves.

Discussion

Influence of physiological condition and anaesthesia on DW-fMRI signal changes for the rat forepaw electrostimulation model

It is well known that modulation of the blood gases, in particular $PaCO_2$, can influence the amplitude of the functional response (Prielmeier et al., 1994; Hsu et al., 1998; Sicard and Duong, 2005; Ramos-Cabrer et al., 2005). It was therefore important to keep the physiological state of the animal stable during the 5–6 h of

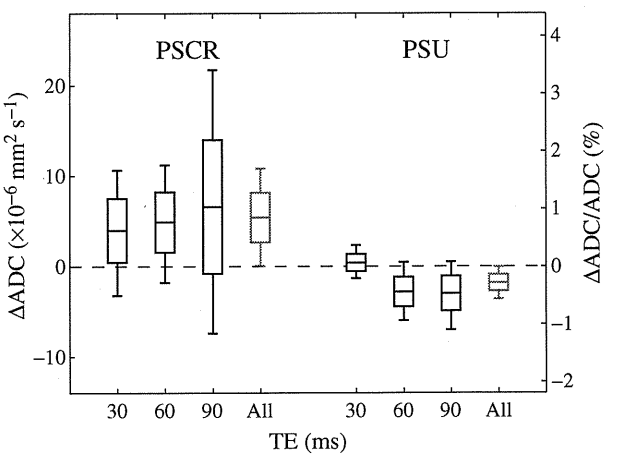

Fig. 4. Box-whisker plots of the ΔADC estimates for each TE after fitting Eq. (5) to the data in Fig. 3. The boxes represent the standard deviation of the estimates and the thinner bars are the 95% confidence intervals. The estimates for the data pooled over all TEs (denoted by All) are drawn in grey. For the purpose of constructing the % signal-change scale on the right-hand axis, the baseline ADC was estimated to be $[637 \pm 28 (594, 705)] \times 10^{-6}$ mm^{2}s^{-1}.

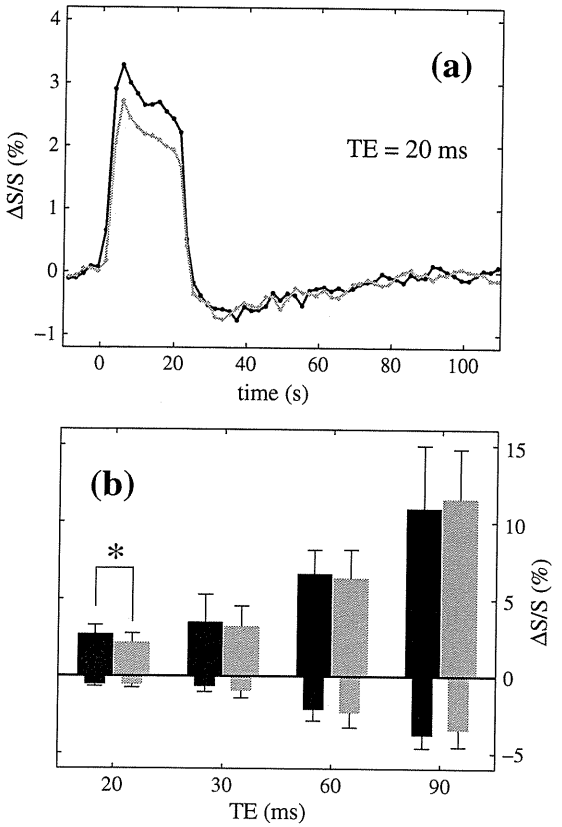

Fig. 5. Comparison of the $b=0$ (black) and $b=200$ (light grey) data. (a) Mean time-courses observed for the TE 20 ms DW-fMRI experiments. The same stimulus paradigm and analysis intervals apply as for the data in Fig. 2. (b) Comparison of the PSCRs (broad upper bars) and PSUs (slim lower bars) for all TEs. No significant difference was found for the TE 30–90 ms data, or for the PSU of the 20 ms data. A weakly significant difference ($p=0.058<0.1$) was found for the PSCR of the TE 20 ms time-course.

experimentation. For this purpose, the animal condition was monitored throughout all experiments with occasional minor adjustments to the ventilation parameters. It should also be noted that the presentation order of the *b*-values was randomised so as to reduce the influence of blood-gas fluctuations on the mean behaviour. In comparison to fMRI studies with the same anaesthetic and similar rat models (Ueki et al., 1992; Hsu et al., 1998; Grüne et al., 1999; Kida et al., 2001; Austin et al., 2005), the physiological readings made during the present experiments were within acceptable normal limits.

As well as the stability of the physiological state, the effect of the anaesthesia on the functional response is also important. Comparison of conscious and anaesthetised animals has found differences in the amplitude of the functional response (Austin et al., 2005; Peeters et al., 2001; Sicard et al., 2003; Brevard et al., 2003; Tsurugizawa et al., 2010). It is also widely recognised that different drugs produce different levels of response according to the dose and characteristics of the stimulus (Huttunen et al., 2008; Weber et al., 2006; Liu et al., 2004; Sommers et al., 2009; Hyder et al., 2002; Maandag et al., 2007; Nakao et al., 2001; Masamoto et al., 2007). In contrast to the α-chloralose-based protocol used here, the subjects in previous high-*b*-value DW-fMRI studies were either awake and aware during experiments (humans), or anaesthetised with isoflurane (cats). Even though it is conceivable that the properties of α-chloralose may have altered the response in some way so that it differed from previously reported DW-fMRI behaviour, no significant correlation was found between either the PSCR or PSU amplitudes and the physiology measurements.

Intravascular signal

A mechanism universally recognised as important in DW-fMRI is the differential attenuation of blood signal in comparison to tissue. This can happen in two ways: (*i*) the higher diffusion coefficient of blood water and the intravoxel incoherent motion of the blood in the vessels combine to attenuate blood signal more strongly in the presence of MPGs (Le Bihan et al., 1998; Callaghan, 1991), and (*ii*) the different field dependence of the transverse relaxation times of the vascular and tissue compartments means that at high field the contribution of deoxygenated blood may be substantially reduced. These effects have been demonstrated in a number of DW-fMRI experiments. For example, for humans at 7 T it has been found that the IV contribution at TE = 32 ms accounts for approximately 20% of the functional signal (Duong et al., 2003). At lower fields where the blood contribution is even more significant, experiments on humans (Jochimsen et al., 2004; Duong et al., 2003; Song et al., 1996) and rats (Duong and Kim, 2000) have demonstrated that the majority of

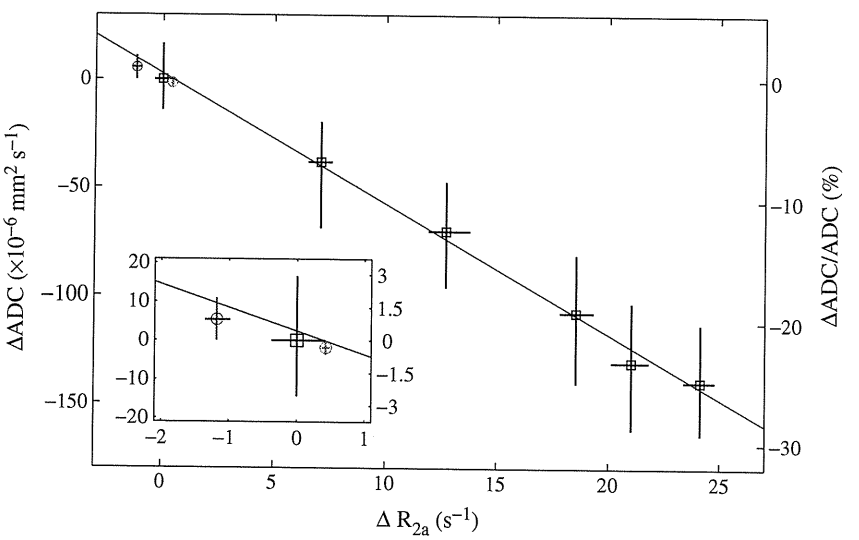

Fig. 6. ΔADC plotted against ΔR_{2a} for the USPIO experiments. The horizontal and vertical bars represent the 95% confidence intervals estimated for ΔR_{2a} and ΔADC, respectively, at each USPIO concentration. The straight line fitted to the data has the form $\Delta ADC = (-6.01 \pm 0.31) \times 10^{-6}\ \Delta R_{2a} + (2.5 \pm 5.2) \times 10^{-6}$. Also plotted are the ($\Delta R_{2a}$, ΔADC) pairs estimated for the PSCR (blue circle) and PSU (red circle) of the functional data after pooling. *Inset*: Expanded view of the PSCR and PSU results.

the IV signal is attenuated quite strongly by even relatively low b-values ($\leq$200–300 s/mm^2). In contrast, for rats at the higher field of 9.4 T the functional signal was independent of b-value in the range 0–500 s/mm^2, which was interpreted as indicating that the signal from large vessels was negligible because the 40 ms TE was very long relative to the T_{2a} of venous blood (Lee et al., 1999).

These effects were investigated in Fig. 5b for the rat forepaw electrostimulation model at 7 T. The TE = 30 ms data in this figure demonstrated that even though the mean PSCR decreases by around 10% from $b = 0$ to 200 s/mm^2, the difference was not significant. There was similarly no significant difference for the TE = 60 and 90 ms data, but there was a weakly significant decrease for the TE = 20 ms data. These results suggest that inside the selected ROIs there is a small residual IV contribution at TE = 20 ms, but for TE $\geq$ 30 ms the blood signal is negligible.

Interpretation of DW-fMRI signal changes for the rat forepaw electrostimulation model

The high b-value DW-fMRI results presented in this manuscript for the rat forepaw electrostimulation model are quite different to those presented in most studies of humans (Darquie et al., 2001; Le Bihan et al., 2006; Miller et al., 2007; Kershaw et al., 2009; Harshbarger and Song, 2006; Kohno et al., 2009; Aso et al., 2009; Michelich et al., 2006) and domestic cats (Jin et al., 2006a,b; Jin and Kim, 2008; Yacoub et al., 2008). With reference to the existing interpretations for DW-fMRI, as the PSCR did not increase with b-value nor did comparison of the $b = 0$ and 2000 s/mm^2 time-courses support a faster onset of the response at high b-value, there is no indication that the cell-swelling mechanism is contributing to the signal. Nor is there any evidence that the PSCR and PSU originate from separate sources, obviating the need for a multicompartmental EV SE-BOLD model (Kershaw et al., 2009). In short, as the functional signal change was relatively insensitive to diffusion-weighting for all analysis intervals (Fig. 3), the data displayed no signature characteristics that strongly suggest multi-compartmental behaviour. Therefore, in accordance with Eq. (3), the simplest explanation for the present data is a signal model that is dominated by a single compartment. As it was concluded in the previous section that the IV signal is negligible for TE $\geq$ 30 ms, the most likely candidate for this compartment is brain tissue, with the source of the functional signal change corresponding to the EV SE-BOLD effect because the PSCR amplitude increases linearly with TE (Duong et al., 2003; Yacoub et al., 2003; Lee et al., 1999), and the behaviour of the signal with b implies that the origin of the signal at high b-value is the same as that at $b = 0$.

Implicit in this interpretation is the assumption that the CSF does not contribute to the functional signal. Recent work has directly demonstrated a functional-like decrease in the CSF volume fraction during stimulation (Jin and Kim, 2010). Presumably the CSF acts as a buffer to accommodate vessel dilation. However, it is unlikely that this mechanism contributes to the present data because the surface of the rat brain over the somatosensory cortex does not contain the prominent gyri and sulci that allow significant partial-voluming with CSF deep in the brains of larger animals. Moreover, care was taken to avoid selecting activated pixels near the surface that might contain substantial CSF fractions.

As a final remark for this section, even though direct comparison should be cautious because the animal and sensory models are very different to those used here, recent work at 4 T on humans is noted (Waggoner et al., 2010). Using both dual-SE (TE = 100 ms) and stimulated-echo sequences (effective TE = 42 ms), that work also found that the signal change did not increase at high b-values. The results were interpreted as indicating that at 4 T the signal contains minimal IV signal at all b-values for the dual-SE sequence, and at $b \geq 600$ s/mm^2 for the stimulated-echo sequence.

Possible influence of gradient coupling on diffusion-weighted functional signal

Whilst fitting Eq. (5) to the data of Fig. 3 found that the estimates of ΔADC as a function of TE were insignificantly different from zero, after combining the data across TEs the improved statistics suggested that the PSCR and PSU gradually decrease and increase, respectively, as b increases (Fig. 4). In particular, the ADC may have increased by around 0.9% for the PSCR. Even though Yacoub et al. (2008) and Jin and Kim (2008) both reported values of this order when calculating ΔADC with a low b-value pair, the ΔADC was actually negative when high b-value data was used. This switching behaviour cannot occur for the present data because the putative trend for the PSCR amplitude is a monotonic decrease over 0–2000 s/mm^2.

If the trends for the PSCR and PSU genuinely exist, one interpretation is the presence of a second signal source. In that case, a conflict with the above single-compartment interpretation of the functional data would have to be acknowledged, although the behaviour of the signal change with b-value would still differ from that in previous high b-value DW-fMRI studies. On the other hand, the gradient-coupling simulations performed by Pampel et al. (2010) suggest that the PSCR would decrease with increasing b-value and the ΔADC would be in the range 0.2–1.2%. Therefore, rather than implying the presence of a second signal source, another potential explanation for the behaviour is the coupling of the background gradients and the applied MPGs.

Recognising that gradient coupling may interfere with the desired signal behaviour, most previous high-b-value DW-fMRI studies have used a dual-SE sequence to minimise the potential influence of this mechanism (Pampel et al., 2010; Jin and Kim, 2008). In contrast, the data presented in this manuscript was intentionally acquired with a single-SE sequence so that the effects of coupling could be investigated with the more flexible rat forepaw electrostimulation model. This was achieved by injecting USPIO into the bloodstream to alter the IV–EV susceptibility difference. Although the injection of USPIO does not really simulate the conditions during functional experiments because there are no concurrent cerebral blood flow or volume changes, the results serve as an empirical estimate of how much the SE-BOLD signal change might be perturbed by the gradient coupling mechanism. The results of the USPIO experiments demonstrated that the functional (ΔR_{2a}, ΔADC) pairs for the PSCR and PSU are compatible with changes to the same parameters in the presence of USPIO (Fig. 6). This suggests that, instead of competing signals from two or more compartments, interaction of the internal gradients with the applied MPGs could be responsible for the small DW-fMRI signal changes with increasing b-value, in which case no conflict with the single-compartment interpretation would occur.

Conclusion

DW-fMRI experiments were performed on a rat forepaw electrostimulation model at 7 T with a single-SE EPI sequence. An advantage of this rat model over humans is that longer experiments can be performed over a wider range of acquisition parameters. The model also uses electric stimulation so that both the stimulus type and brain-sensory system differ from previous high b-value DW-fMRI studies. A possible disadvantage is the use of anaesthesia, muscle relaxant and other drugs that could adversely influence the physiological response and hence functional signal. Modifications to the functional response with respect to TE in the range 30–90 ms and b-value in the range 0–2000 s/mm^2 were evaluated for the PSCR and PSU intervals. There was no strong dependence of the signal change on b-value for either interval or any of the TEs. Similarly, no clear dependence of ΔR_{2a} on b-value was observed. Even though there may be a small residual IV contribution at TE = 20 ms, the absence of clear signal attenuation with increasing b-value suggested

that there is no significant blood contribution to the functional signal for TE ≥ 30 ms. Overall, the data contained none of the characteristics found in previous high *b*-value DW-fMRI studies that suggest multicompartmental behaviour. The simplest interpretation for the data over the range of acquisition parameters used in the study is a single-compartment signal model, with the most likely candidate for the signal origin being EV SE-BOLD. The functional changes to ADC and R_{2a} were compatible with those observed in resting-state experiments with USPIO, which suggests that at 7 T and within the range of parameters used, no mechanism other than the influence of gradient coupling is needed to sufficiently explain small DW-fMRI signal changes with increasing *b*-value.

Acknowledgments

The authors would like to thank Takeo Shimomura for technical assistance, as well as Daigo Kuroiwa and Kazuto Masamoto for valuable discussion during the preparation of this manuscript. This research was supported by a Grant-in-Aid for Scientific Research (C) (#21613010) and a Grant-in-Aid for Scientific Research (B) (#21390352) from the Japan Society for the Promotion of Science (JSPS). It was also partially supported by the JSPS through its "Funding Program for World-Leading Innovative R&D on Science and Technology (FIRST Program)." One of the authors (JAAA) was also partially funded by a grant from the Scandinavia-Japan Sasakawa Foundation.

References

Aso, T., Urayama, S., Poupon, C., Sawamoto, N., Fukuyama, H., Le Bihan, D., 2009. An intrinsic diffusion response function for analyzing diffusion functional MRI time series. Neuroimage 47, 1487–1495.

Austin, V.C., Blamire, A.M., Allers, K.A., Sharp, T., Styles, P., Matthews, P.M., Sibson, N.R., 2005. Confounding effects of anesthesia on functional activation in rodent brain: a study of halothane and α-chloralose anesthesia. Neuroimage 24, 92–100.

Brevard, M.E., Duong, T.Q., King, J.A., Ferris, C.F., 2003. Changes in MRI signal intensity during hypercapnic challenge under conscious and anesthetized conditions. Magn. Reson. Imaging 21, 995–1001.

Callaghan, P.T., 1991. Principles of Nuclear Magnetic Resonance Spectroscopy. Oxford University Press, New York, p. 362.

Darquie, A., Poline, J.B., Poupon, C., Saint-Jalmes, H., Le Bihan, D., 2001. Transient decrease in water diffusion observed in human occipital cortex during visual stimulation. Proc. Natl. Acad. Sci. USA 98 (16), 9391–9395.

Does, M.D., Zhong, J., Gore, J.C., 1999. In vivo measurement of ADC changes due to intravascular susceptibility variation. Magn. Reson. Med. 41, 236–240.

Duong, T.Q., Kim, S.-G., 2000. In vivo MR measurements of regional arterial and venous blood volume fractions in intact rat brain. Magn. Reson. Med. 43, 393–402.

Duong, T.Q., Yacoub, E., Adriany, G., Hu, X., Ugurbil, K., Kim, S.-G., 2003. Microvascular BOLD contribution at 4 T and 7 T in the human brain: gradient-echo and spin-echo fMRI with suppression of blood effects. Magn. Reson. Med. 49, 1019–1027.

Efron, B., Tibshirani, R.J., 1994. An Introduction to the Bootstrap. Chapman & Hall/CRC.

Gangstead, S.L., Song, A.W., 2002. On the timing characteristics of the apparent diffusion coefficient contrast in fMRI. Magn. Reson. Med. 48, 385–388.

Grüne, M., Pillekamp, F., Schwindt, W., Hoehn, M., 1999. Gradient echo time dependence and quantitative parameter maps for somatosensory activation in rats at 7 T. Magn. Reson. Med. 42, 118–126.

Harshbarger, T.B., Song, A.W., 2006. Endogenous functional CBV contrast revealed by diffusion weighting. NMR Biomed. 19, 1020–1027.

Hsu, E.W., Hedlund, L.W., MacFall, J.R., 1998. Functional MRI of the rat somatosensory cortex: effects of hyperventilation. Magn. Reson. Med. 40, 421–426.

Huttunen, J.K., Grohn, O., Penttonen, M., 2008. Coupling between simultaneously recorded BOLD response and neuronal activity in the rat somatosensory cortex. Neuroimage 39, 775–785.

Hyder, F., Rothman, D.L., Shulman, R.G., 2002. Total neuroenergetics support localized brain activity: implications for the interpretation of fMRI. Proc. Natl. Acad. Sci. USA 99, 10771–10776.

Jin, T., Kim, S.-G., 2008. Functional changes of apparent diffusion coefficient during visual stimulation investigated by diffusion-weighted gradient-echo fMRI. Neuroimage 41, 801–812.

Jin, T., Kim, S.-G., 2010. Change of the cerebrospinal fluid volume during brain activation investigated by $T_{1\rho}$-weighted fMRI. Neuroimage 51, 1378–1383.

Jin, T., Wang, P., Tasker, M., Zhao, F., Kim, S.-G., 2006a. Source of nonlinearity in echo-time-dependent BOLD fMRI. Magn. Reson. Med. 55, 1281–1290.

Jin, T., Zhao, F., Kim, S.-G., 2006b. Sources of functional apparent diffusion coefficient changes investigated by diffusion-weighted spin-echo fMRI. Magn. Reson. Med. 56, 1283–1292.

Jochimsen, T.H., Norris, D.G., Mildner, T., Möller, H.E., 2004. Quantifying the intra- and extravascular contributions to spin-echo fMRI at 3 T. Magn. Reson. Med. 52, 724–732.

Keilholz, S.D., Silva, A.C., Raman, M., Merkle, H., Koretsky, A.P., 2006. BOLD and CBV-weighted functional magnetic resonance imaging of the rat somatosensory system. Magn. Reson. Med. 55, 316–324.

Kennan, R.P., Scanley, B.E., Innis, R.B., Gore, J.C., 1998. Physiological basis for BOLD MR signal changes due to neuronal stimulation: separation of blood volume and magnetic susceptibility effects. Magn. Reson. Med. 40, 840–846.

Kershaw, J., Ardekani, B.A., Kanno, I., 1999. Application of Bayesian inference to fMRI data analysis. IEEE Trans. Med. Imaging 18 (12), 1138–1153.

Kershaw, J., Tomiyasu, M., Kashikura, K., Hirano, Y., Nonaka, H., Hirano, M., Ikehira, H., Kanno, I., Obata, T., 2009. A multi-compartmental SE-BOLD interpretation for stimulus-related signal changes in diffusion-weighted functional MRI. NMR Biomed. 22, 770–778.

Kida, I., Hyder, F., Behar, K.L., 2001. Inhibition of voltage-dependent sodium channels suppresses the functional magnetic resonance imaging response to forepaw somatosensory activation in the rodent. J. Cereb. Blood Flow Metab. 21 (5), 585–591.

Kohno, S., Sawamoto, N., Urayama, S., Aso, T., Aso, K., Seiyama, A., Fukuyama, H., Le Bihan, D., 2009. Water-diffusion slowdown in the human visual cortex on visual stimulation precedes vascular responses. J. Cereb. Blood Flow Metab. 29, 1197–1207.

Kuroiwa, D., Kawaguchi, H., Kershaw, J., Tachibana, A., Autio, J., Hirano, M., Aoki, I., Kanno, I., Obata, T., 2009. Signal source in heavily diffusion-weighted functional MRI. Proc 17th ISMRM 1571.

Le Bihan, D., Breton, E., Lallemand, D., Aubin, M.-L., Vignaud, J., Laval-Jeantet, M., 1998. Separation of diffusion and perfusion in intravoxel incoherent motion MR imaging. Radiology 168, 497–505.

Le Bihan, D., Urayama, S., Aso, T., Hanakawa, T., Fukuyama, H., 2006. Direct and fast detection of neuronal activation in the human brain with diffusion MRI. Proc. Natl. Acad. Sci. USA 103 (21), 8263–8268.

Lee, S.-P., Silva, A.C., Ugurbil, K., Kim, S.-G., 1999. Diffusion-weighted spin-echo fMRI at 9.4 T: microvascular/tissue contribution to BOLD signal changes. Magn. Reson. Med. 42, 919–928.

Lee, S.-P., Silva, A.C., Kim, S.-G., 2002. Comparison of diffusion-weighted high-resolution CBF and spin-echo BOLD fMRI at 9.4 T. Magn. Reson. Med. 47, 736–741.

Liu, Z.M., Schmidt, K.F., Sicard, K.M., Duong, T.Q., 2004. Imaging oxygen consumption in forepaw somatosensory stimulation in rats under isoflurane anaesthesia. Magn. Reson. Med. 52, 277–285.

Maandag, N.J., Coman, D., Sanganahalli, B.G., Herman, P., Smith, A.J., Blumenfeld, H., Shulman, R.G., Hyder, F., 2007. Energetics of neuronal signaling and fMRI activity. Proc. Natl. Acad. Sci. USA 104, 20546–20551.

Mandeville, J.B., Marota, J.J.A., 1999. Vascular filters of functional MRI: spatial localization using BOLD and CBV contrast. Magn. Reson. Med. 42, 591–598.

Masamoto, K., Kim, T., Fukuda, M., Wang, P., Kim, S.-G., 2007. Relationship between neural, vascular, and BOLD signals in isoflurane-anesthetized rat somatosensory cortex. Cereb. Cortex 17, 942–950.

Michelich, C.R., Song, A.W., MacFall, J.R., 2006. Dependence of gradient-echo and spin-echo BOLD fMRI at 4 T on diffusion-weighting. NMR Biomed. 19, 566–572.

Miller, K.L., Bulte, D.P., Devlin, H., Robson, M.D., Wise, R.G., Woolrich, M.W., Jezzard, P., Behrens, T.E.J., 2007. Evidence for a vascular contribution to diffusion fMRI at high *b*-value. Proc. Natl. Acad. Sci. USA 104 (52), 20967–20972.

Nakao, Y., Itoh, Y., Kuang, T.-Y., Cook, M., Jehle, J., Sokoloff, L., 2001. Effects of anesthesia on functional activation of cerebral blood flow and metabolism. Proc. Natl. Acad. Sci. USA 98 (13), 7593–7598.

Pampel, A., Jochimsen, T.H., Möller, H.E., 2010. BOLD background gradient contributions in diffusion-weighted fMRI—comparison of spin-echo and twice-refocused spin-echo sequences. NMR Biomed. 23 (6), 610–618.

Peeters, R.R., Tindemans, I., De Schutter, E., Van der Linden, A., 2001. Comparing BOLD fMRI signal changes in the awake and anesthetized rat during electrical forepaw stimulation. Magn. Reson. Imaging 19, 821–826.

Prielmeier, F., Nagatomo, Y., Frahm, J., 1994. Cerebral blood oxygenation in rat brain during hypoxic hypoxia. Quantitative MRI of effective transverse relaxation rates. Magn. Reson. Med. 31, 678–681.

Ramos-Cabrer, P., Weber, R., Wiedermann, D., Hoehn, M., 2005. Continuous noninvasive monitoring of transcutaneous blood gases for a stable and persistent BOLD contrast in fMRI studies in the rat. NMR Biomed. 18, 440–446.

Sicard, K.M., Duong, T.Q., 2005. Effects of hypoxia, hyperoxia, and hypercapnia on baseline and stimulus-evoked BOLD, CBF, and $CMRO_2$ in spontaneously breathing animals. Neuroimage 25, 850–858.

Sicard, K., Shen, Q., Brevard, M.E., Sullivan, R., Ferris, C.F., King, J.A., Duong, T.Q., 2003. Regional cerebral blood flow and BOLD responses in conscious and anesthetized rats under basal and hypercapnic conditions: implications for functional MRI studies. J. Cereb. Blood Flow Metab. 23, 472–481.

Sommers, M.G., van Egmond, J., Booij, L.H.D.J., Heerschap, A., 2009. Isoflurane anesthesia is a valuable alternative for α-chloralose anesthesia in the forepaw stimulation model in rats. NMR Biomed. 22, 414–418.

Song, A.W., Wong, E.C., Tan, S.G., Hyde, J.S., 1996. Diffusion-weighted fMRI at 1.5 T. Magn. Reson. Med. 35, 155–158.

Song, A.W., Woldorff, M.G., Gangstead, S., Mangun, G.R., McCarthy, G., 2002. Enhanced spatial localization of neuronal activation using simultaneous apparent-diffusion-coefficient and blood-oxygenation functional magnetic resonance imaging. Neuroimage 17, 742–750.

Stesjkal, E.G., Tanner, J.E., 1965. Spin diffusion measurements: spin echoes in the presence of a time-dependent field gradient. J. Chem. Phys. 42 (1), 288–292.

Tsurugizawa, T., Uematsu, A., Uneyama, H., Torii, K., 2010. Effects of isoflurane and alpha-chloralose anesthesia on BOLD fMRI responses to ingested L-glutamate in rats. Neuroscience 165 (1), 244–251.

Ueki, M., Mies, G., Hossmann, K.A., 1992. Effect of alpha-chloralose, halothane, pentobarbital and nitrous oxide anesthesia on metabolic coupling in somatosensory cortex of rat. Acta Anesthesiol. Scand. 36 (4), 318–322.

Waggoner, R.A., Tanaka, K., Cheng, K., 2010. Investigating the origins of the DfMRI signal at 4 Tesla. Proc 18th ISMRM 1120.

Weber, R., Ramos-Cabrer, P., Wiedermann, D., van Camp, N., Hoehn, M., 2006. A fully noninvasive and robust experimental protocol for longitudinal fMRI studies in the rat. Neuroimage 29, 1303–1310.

Yacoub, E., Duong, T.Q., Van De Moortele, P.-F., Lindquist, M., Adriany, G., Kim, S.-G., Ugurbil, K., Hu, X., 2003. Spin-echo fMRI in humans using high spatial resolutions and high magnetic fields. Magn. Reson. Med. 49, 655–664.

Yacoub, E., Uludag, K., Ugurbil, K., Harel, N., 2008. Decreases in ADC observed in tissue areas during activation in the cat visual cortex at 9.4 T using high diffusion sensitization. Magn. Reson. Imaging 26, 889–896.

Zhong, J., Kennan, R.P., Gore, J.C., 1991. Effects of susceptibility variations on NMR measurements of diffusion. J. Magn. Reson. 95, 267–280.

Zhong, J., Kennan, R.P., Fulbright, R.K., Gore, J.C., 1998. Quantification of intravascular and extravascular contributions to BOLD effects induced by alteration in oxygenation or intravascular contrast agents. Magn. Reson. Med. 40, 526–536.

BRAIN RESEARCH 1369 (2011) 103–111

available at www.sciencedirect.com

ScienceDirect

www.elsevier.com/locate/brainres

BRAIN RESEARCH

Research Report

Reproducibility and variance of a stimulation-induced hemodynamic response in barrel cortex of awake behaving mice

Hiroyuki Takuwa[a,1,2,3,4], *Joonas Autio*[a,2,4,5], *Haruka Nakayama*[a,b,2,4], *Tetsuya Matsuura*[a,c,6], *Takayuki Obata*[a,6], *Eiji Okada*[b,1], *Kazuto Masamoto*[a,d,*,1,2,3,4], *Iwao Kanno*[a,1,3]

[a]*Department of Biophysics, Molecular Imaging Center, National Institute of Radiological Sciences, 4-9-1 Anagawa, Chiba 263-8555, Japan*
[b]*Department of Electronics and Electrical Engineering, Keio University, 3-14-1 Hiyoshi, Kohoku-ku, Yokohama 223-8522, Japan*
[c]*Academic Group of Mathematical and Natural Science, Iwate University, 4-3-5 Ueda, Morioka 020-8551, Japan*
[d]*Center for Frontier Science and Engineering, University of Electro-Communications, 1-5-1 Chofugaoka, Chofu, Tokyo 182-8585, Japan*

ARTICLE INFO

Article history:
Accepted 3 November 2010
Available online 9 November 2010

Keywords:
Cerebral blood flow
Laser–Doppler flowmetry
Neurovascular coupling
Functional plasticity
Somatosensory cortex

ABSTRACT

The present work evaluated the reproducibility and variance of the cerebral blood flow (CBF) response to natural whisker stimulation in the barrel cortex of awake behaving mice. The animal was placed on an air float ball that allowed the animal to walk, while the head of the animal was fixed in a custom-made stereotactic apparatus. Dynamic CBF changes in the barrel cortex and animal locomotion were simultaneously monitored with laser–Doppler flowmetry (LDF) and an optical motion sensor that detected the rotation distance of the ball, respectively. Whisker stimulation-induced CBF measured under daytime and nighttime conditions showed consistent responses (24% and 23% of the pre-stimulus baseline, respectively), whereas the amount of locomotion was 1.4 times higher during nighttime relative to daytime. Repeated longitudinal experiments over 7 days showed a reproducible, evoked CBF (13–26% relative to the baseline among 7 animals). The mean of the variance coefficient (i.e., standard deviation divided by mean) across multiple days was 0.11 and 0.75 for evoked CBF and locomotion, respectively. These results showed reproducible and reliable measurements of longitudinal CBF response in behaving mice regardless of day-to-day variations in locomotion. Furthermore, we confirmed that the CBF response to whisker stimulation was well localized and reproducible, measured with laser speckle imaging under awake condition. The results further show the capability of long-term hemodynamic imaging in normal and disease-

* *Corresponding author*. Center for Frontier Science and Engineering, University of Electro-Communications, 1-5-1 Chofugaoka, Chofu, Tokyo 182-8585, Japan. Fax: +81 42 443 5930.
E-mail address: masamoto@mce.uec.ac.jp (K. Masamoto).
[1] Designed research.
[2] Performed research.
[3] Wrote the paper.
[4] Analyzed data.
[5] Present address: Department of Neurobiology, A. I. Virtanen Institute, University of Kuopio, Kuopio, Finland.
[6] Helped data interpretation and discussion.

0006-8993/$ – see front matter
doi:10.1016/j.brainres.2010.11.007

model mice, which is of particular importance for understanding the longitudinal changes and plasticity of neurovascular coupling and behavioral performances such as during growth, development and aging.

1. Introduction

Neurovascular coupling is a fundamental process in the maintenance of normal brain function. Previous studies have attempted to understand the coupling between neural and vascular properties using *in vitro* slices and *in vivo* acute experimental models (Boorman et al., 2010; Cauli et al., 2004; Chaigneau et al., 2007; Enager et al., 2009; Lauritzen, 2001; Peppiatt et al., 2006; Shi et al., 2008; Takano et al., 2006; Zonta et al., 2003). Nevertheless, signaling pathways from neural events, such as spiking and/or synaptic activity, to vascular events, such as arterial vasodilation and/or decrease in resistance to red blood cell flow, remain incompletely understood. Additionally, the previously published studies have been conducted rather under steady state conditions, which hamper the understanding of longitudinal changes in neurovascular coupling. For example, whether dysregulation of neurovascular coupling contributes to the pathogenesis of neurodegenerative disorders remains an unanswered (Carmignoto and Gómez-Gonzalo, 2010; Lok et al., 2007; Zacchigna et al., 2008). To further understand the dynamic processing and related pathogenesis of central neurodegeneration, it is therefore important to examine the interactive evolution of neurovascular coupling from longitudinal perspectives, including such as during growth, development, and aging.

It has been shown that a development of a cerebrovascular response to neural activity lags behind an emergence of electrophysiological activity during the early postnatal period (Colonnese et al., 2008). The finding indicates a delayed formation of neurovascular coupling, which could be due to slow development of vascular reactivity and/or mediator functionality to convey neural signals to vascular reactions. On the other hand, an age-related reduction of cerebral blood flow (CBF) was known to be associated with a decline in cognitive function (Goldman et al., 1987). Later studies have suggested that the limited supply for metabolic demand is considered a key factor in the age-related decline in neural function (Riddle et al., 2003). A breakdown of microvascular networks has also been found to take place in advance of the accumulation of amyloidal plaque in a mouse model of Alzheimer's disease (Meyer et al., 2008). These studies indicate an importance for long-term investigation of the plastic changes of neurovascular coupling and associated behavioral performances with stable and reproducible animal models.

In the present study, an awake mice model was established to explore the long-term behavior of CBF and animal locomotion repeatedly while maintaining a relatively natural environment. We used laboratory mice for a series of experiments because this animal has advantages in the availability of genetically engineered disease models. The CBF response to air puff-produced whisker stimulation (10 Hz and 20 s) were examined under unanesthetized conditions because neurovascular responses are critically modulated by anesthetic agents and depths which potentially affect the reproducibility of the results (Masamoto et al., 2007; Masamoto et al., 2009). First we performed simultaneous recordings of CBF and locomotion measured with laser–Doppler flowmetry and optical motion sensor, respectively (see Fig. 1), under either daytime or nighttime conditions (*Experiment I*), to determine possible confounders arising from circadian variations in the animals (Wauschkuhn et al., 2005). We then evaluated the reproducibility and variance of the CBF response to whisker stimulation over a week, while the animals experienced a normal life between the recordings (*Experiment II*). Finally, the CBF mapping experiment was carried out with

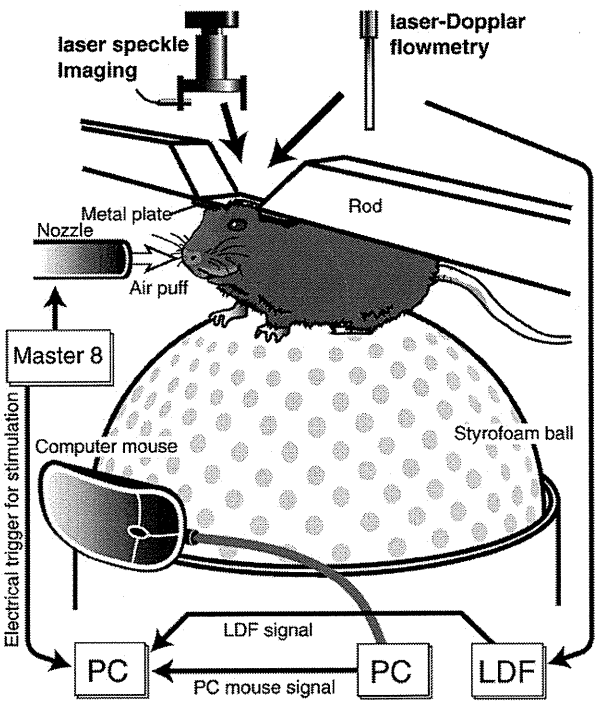

Fig. 1 – Experimental arrangement. A custom-made metal plate was attached to the animal skull and the head was fixed on a rod of a stereotactic instrument. The animal was secured on a styrofoam ball which is floated on an air jet from the bottom and the animal was allowed to walk freely on it. The rotation distance of the ball was measured with an optical computer mouse to detect animal locomotion. Either laser speckle imaging or laser–Doppler flowmetry (LDF) was performed to measure CBF in the somatosensory barrel cortex. Analog outputs converted from the computer mouse and LDF signals were recorded with a polygraph system equipped to a personal computer (PC) and synchronized with a pulse generator (Master 8) that controlled the air puff stimulation.